ARMY RESEARCH LABORATORY

Computer Models of the Human Body Signature for Sensing Through the Wall Radar Applications

by Traian Dogaru, Lam Nguyen, and Calvin Le

ARL-TR-4290 **September 2007**

NOTICES

Disclaimers

The findings in this report are not to be construed as an official Department of the Army position unless so designated by other authorized documents.

Citation of manufacturer's or trade names does not constitute an official endorsement or approval of the use thereof.

Destroy this report when it is no longer needed. Do not return it to the originator.

Army Research Laboratory
Adelphi, MD 20783-1197

ARL-TR-4290 **September 2007**

Computer Models of the Human Body Signature for Sensing Through the Wall Radar Applications

Traian Dogaru, Lam Nguyen, and Calvin Le
Sensors and Electron Devices Directorate, ARL

REPORT DOCUMENTATION PAGE

Form Approved
OMB No. 0704-0188

1. REPORT DATE *(DD-MM-YYYY)*	2. REPORT TYPE	3. DATES COVERED (From - To)
September 2007	Final	2005 to 2007

4. TITLE AND SUBTITLE
Computer Models of the Human Body Signature for Sensing Through the Wall Radar Applications

5a. CONTRACT NUMBER

5b. GRANT NUMBER

5c. PROGRAM ELEMENT NUMBER

6. AUTHOR(S)
Traian Dogaru, Lam Nguyen, and Calvin Le

5d. PROJECT NUMBER

5e. TASK NUMBER

5f. WORK UNIT NUMBER

7. PERFORMING ORGANIZATION NAME(S) AND ADDRESS(ES)
U.S. Army Research Laboratory
ATTN: AMSRD-ARL-SE-RU
2800 Powder Mill Road
Adelphi, MD 20783-1197

8. PERFORMING ORGANIZATION REPORT NUMBER
ARL-TR-4290

9. SPONSORING/MONITORING AGENCY NAME(S) AND ADDRESS(ES)
U.S. Army Research Laboratory
2800 Powder Mill Road
Adelphi, MD 20783-1197

10. SPONSOR/MONITOR'S ACRONYM(S)

11. SPONSOR/MONITOR'S REPORT NUMBER(S)
ARL-TR-4290

12. DISTRIBUTION/AVAILABILITY STATEMENT
Approved for public release; distribution unlimited.

13. SUPPLEMENTARY NOTES

14. ABSTRACT
This technical report presents numerical simulations of the human body radar signature, with application to sensing through the wall (STTW) scenarios. We utilize the Finite Difference Time Domain (FDTD) modeling technique to compute the electromagnetic scattering from realistic human body models. We analyze the radar cross section (RCS) of the human body in different configurations as a function of aspect angle, frequency, and polarization, drawing important conclusions in terms of the magnitude, variability, and statistics of the human radar signature. We also use the modeling data in order to simulate the operation of a low frequency, ultra-wideband (UWB) synthetic aperture radar (SAR), by creating SAR images of the human body in various configurations. The results obtained in this study can be used as guidance by radar system designers in order to optimize performance in the context of a STTW scenario.

15. SUBJECT TERMS
Radar, sensing through the wall, computational electromagnetics, human body

16. SECURITY CLASSIFICATION OF:			17. LIMITATION OF ABSTRACT	18. NUMBER OF PAGES	19a. NAME OF RESPONSIBLE PERSON
a. REPORT	b. ABSTRACT	c. THIS PAGE	SAR	56	Traian Dogaru
U	U	U			19b. TELEPHONE NUMBER (*Include area code*) (301) 394-1482

Standard Form 298 (Rev. 8/98)
Prescribed by ANSI Std. Z39.18

Contents

List of Figures

List of Tables

Acknowledgments

This study was partially funded by the Communications-Electronics Research Development and Engineering Center (CERDEC), Intelligence and Information Warfare Directorate (I2WD) at Ft. Monmouth, NJ, and the Office of Naval Research (ONR) in Arlington, VA. The authors would like to thank Dr. Andy Sullivan from the U.S. Army Research Laboratory (ARL) for helpful discussions in interpreting the data and drawing this report's conclusions. They would also like to express their appreciation to Dr. Vijaya Shankar of Hypercomp, Inc., who has provided the Time-Domain Electro-Magnetic Parallel Unstructured Simulator (TEMPUS) simulation results in section 3.2.

1. Introduction

Through the wall sensing has received a great deal of interest during the last few years from defense and law enforcement agencies in many countries, as well as commercial concerns. Among the large spectrum of sensors that have been considered, low-frequency ultra-wideband (UWB) radar offers great potential for detecting targets behind walls, as well as for building imaging. The major challenge for this type of scenario, which involves the penetration of the electromagnetic waves through a lossy medium concealing the target, is the trade-off between good penetration properties and good resolution, while trying to maintain a realistic antenna size/power requirement. Operating the radar in the low frequency microwave range (300 MHz to 3 GHz) has the advantage of good penetration through building structures. At the same time, UWB excitation and synthetic aperture radar (SAR) technologies can be employed in order to obtain good image resolution.

At the U.S. Army Research Laboratory (ARL), we are drawing on more than a decade of experience in utilizing UWB radar for detection and imaging of targets in concealed environments, such as foliage penetrating radar (FOPEN) and ground penetrating radar (GPR) (*1*, *2*). We are currently involved in two major sensing through the wall (STTW) programs within Department of Defense (DoD), as well as participating in international panels on STTW technologies with military applications.

Since STTW represents a relatively new application of the UWB radar, a significant amount of research is currently being performed in order to understand the phenomenology and the fundamental limits of this technology. A great part of this research activity consists of computer simulations of various scenarios relevant to this problem. Figure 1 summarizes some of the issues that need to be addressed through computer models. Based on these models, we are able to make recommendations to radar system designers with regard to essential parameters, such as frequency of operation, bandwidth, aperture size, polarization, etc. Also, comparing the simulations with experimental results increases our confidence in the models validity and, at the same time, allows us to better understand the origin of certain subtle effects and artifacts in the experimental setup.

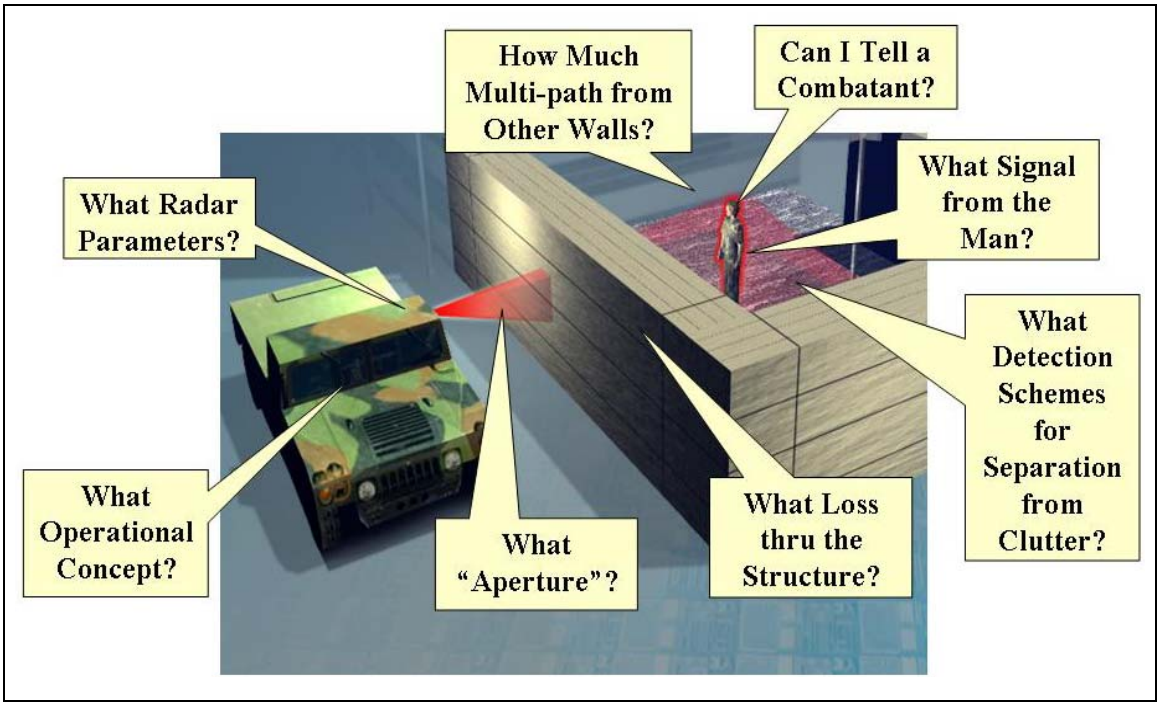

Figure 1. Issues related to STTW radar that are addressed by computer modeling in this report.

A major goal for STTW applications is detecting, identifying, and tracking humans enclosed in building structures. Knowing the expected strength and variability of the radar return from a human is a valuable piece of information for the radar system designer. In this report, we analyze the human body radar signature from a computer modeling perspective. First, we present a short overview of the modeling methods utilized in this study (section 2). The modeling results are presented in section 3. We introduce the computational meshes in section 3.1, and then analyze the human body radar cross section (RCS) in section 3.2 and SAR images of the human body in section 3.3. In section 3.4 we investigate the RCS of a human behind a wall. We finalize with conclusions in section 4.

2. Overview of the Electromagnetic Modeling Techniques

The Finite Difference Time Domain (FDTD) method is currently one of the most prominent techniques in electromagnetic wave modeling. Based on a relatively simple numerical scheme described by Yee in a 1966 paper (*3*), FDTD benefited from the spectacular advances in computer hardware and architecture, as well as the intense research activity in the field of computational electromagnetics (CEM), to become a mainstream modeling technique for wave

phenomena in the 1990s. The literature dedicated to FDTD is mature, and there are a number of reference books containing a comprehensive treatment of the subject (*4*, *5*). In this section, we will summarize a few important aspects of this numerical technique.

The FDTD algorithm is based on discretizing Maxwell's time-domain equations, using finite differences in spatial and temporal dimensions. The computational space, with a uniform, rectangular, grid-like structure, is made of elementary cubic cells. The electromagnetic field components are computed along the cell's edges and faces. They are also computed at discrete time steps. Each cubic cell is assigned the material properties (permittivity ε, permeability μ, and conductivity σ) of the corresponding region in space. By discretizing Maxwell's equations in time and space, we obtain the so-called FDTD update equations, which allow updating of a current field component sample, based on the values of neighboring field component samples obtained at a previous time step. Thus, starting with some known initial values of the field components within the computational space (usually they are initialized with zero), an electromagnetic wave can be propagated through this space by updating the electric and magnetic field samples in a leap-frog manner.

There are a number of advantages that distinguish the FDTD-type algorithms from other major classes of computational electromagnetic techniques, such as Method-of-Moments, the Finite Element Method, or Ray Tracing. FDTD is an exact, full-wave, explicit solver; this last property means that no matrix equation is involved. There is no convergence test involved with FDTD, which means that, provided certain stability conditions are observed, the code will always run through (though that doesn't mean the results are always error-free). FDTD can handle almost arbitrary media electric properties and geometries. The geometry implementation is relatively simple (at least in the most basic implementation form), and there are very few restrictions on topologies, relative positions of targets and ground planes, as well as mixing of various materials inside targets or grids. The excitation can be provided by plane waves (for distant sources) or by antennas, which may be included in the model. Both near-field and far-field can be obtained in an FDTD simulation, although the computational grid only extends in a small region of interest. Since FDTD operates in the time domain, results can be provided over a wide range of frequencies in one time-marching run, at any angle of observation. In terms of programming, the core of the algorithm (the update equations) is easy to implement. Also, the algorithm is an excellent candidate for parallelization, which allows the user to take advantage of the huge computing power available at High-Performance Computing (HPC) Centers.

There are also disadvantages associated with the class of algorithms related to FDTD. The most obvious is the fact that FDTD is very computationally expensive. Since it needs to volumetrically grid up the entire geometry of interest in three dimensions, using a fine meshing unit (the cubic cell), the computational space increases very rapidly with the wave frequency (*f*). Thus, the memory utilized by the code increases with f^3, whereas the central processing unit (CPU) time increases with f^4. However, this problem is mitigated by the tremendous increase in computational power of modern computer systems. Another problem inherent to the FDTD-type

algorithms is the numerical dispersion. This phenomenon is the product of errors in discretizing continuous partial differential equations into finite difference equations; when coupled with the FDTD-specific time-marching process, this leads to phase errors in the field solution that accumulate in time. In order to keep these errors under control, the field spatial sampling rate must be relatively high (the rule of thumb is at least 10 sampling points per wavelength), which explains, in part, why the algorithm is so computational intensive.

FDTD has been used in almost every application of CEM: wave propagation over terrain or manmade structures; antenna and waveguide analysis; radar scattering; optics and opto-electronics; and radio frequency (RF) effects in electronics circuits. Our main interest here is in computing the radar signatures for scenarios related to UWB radar for STTW applications. In these scenarios, a short duration pulse is sent by the transmitter, the wave is scattered by the target, and the time-domain response is captured by the receiver. FDTD allows the computation of the radar signature over the entire frequency band in one run, thus literally simulating the operation of a pulse-based UWB radar.

There are many available implementations of the FDTD algorithm. The code we utilized for this work is called AFDTD and was entirely developed at ARL for radar signature modeling. This is a parallel code for distributed systems, specialized in solving far-field radar scattering problems in a half-space environment (that is, including a dielectric ground plane). AFDTD can import meshes and output data in various formats, compatible with other popular CEM codes. The data visualization was done with either MATLAB (developed by MathWorks, Inc.) or Pioneer RCS (developed by Science Applications International Corporation (SAIC)). The AFDTD code was run at the U.S. Army Major Shared Resource Center (MSRC) (*6*) on several HPC platforms, such as IBM SP3 and SP4 and Linux Networx Evolocity II clusters. The pre- and post-processing were performed on Dell workstations running Windows XP.

3. Numerical Results

The propagation of electromagnetic waves in the presence of the human body has been studied for a long time, relating primarily to medical applications. During the 1990s, concerns about the health effects of electromagnetic radiation within the wireless industry prompted a number of studies trying to evaluate the radiation absorption rates inside the human body in the presence of an electromagnetic energy source. Most of those studies consisted of computer models of the wave propagation inside the body and were made possible by advances in computer hardware, as well as the availability of mature FDTD simulation codes (*7*-*9*). The FDTD method was the natural candidate to modeling this type of problems, given the complexity of human tissues dielectric properties. However, until recently, very little work has been done in modeling the radar signature of the human body. The recent focus on military and national security applications, together with the emergence of the UWB microwave radar as a promising

technology for detecting the human presence in concealed environments, made the evaluation of the human body radar signature a problem of great interest. Such models are very useful in designing and predicting the performance of radar systems for human presence detection.

3.1 Computational Grids

As mentioned in section 2, most FDTD algorithms operate on a three-dimensional rectangular grid made of elementary cells. Each cell is assigned the dielectric properties of the material which occupies that region in space. Therefore, the objects need to be described by a volumetric mesh (as opposed to surface integral equation methods, where only a description of the surface bounding an object is necessary). For the human body modeling we used two different meshes, described in figure 2a and 2b. We found the mesh in figure 2a (that we call the "fat man") on a Web site maintained by the U.S. Air Force Research Laboratory, RF Radiation Branch (Brooks Air Force Base) (*10*). (Unfortunately, the page containing the human body models is no longer available.) The meshes stored at this site represented highly detailed FDTD-compatible grids, where the dielectric properties of each human tissue are sampled using 1 mm, 2 mm, or 3 mm cubic cells. A detailed description of the body tissue dielectric properties was given in reference 11. In this report, the complex relative permittivity is modeled as a complicated function of frequency (4-Cole-Cole model). Since the AFDTD code can only handle materials with frequency-independent dielectric constant and conductivity, throughout our simulations we employed their values computed at a fixed frequency (usually 1 GHz), according to the model in (*11*). The effects of this approximation will be discussed in section 3.2. A cross section through this body model at the torso level is shown in figure 3, where each tissue is represented by a different color. The mesh in figure 2b (that we call the "fit man") was obtained by manipulating the Computer-Aided Design (CAD) model of human body that we obtained from a commercial Web site (*12*). Since this model does not include the internal structure of the body, but only the exterior shell, we must assume that the entire body is made of the same uniform dielectric material. We picked for this material dielectric properties close to those of skin ($\varepsilon_r = 50$, $\sigma = 1$ S/m). While this is only an approximate model, we will later discuss its validity and its implications for our computations.

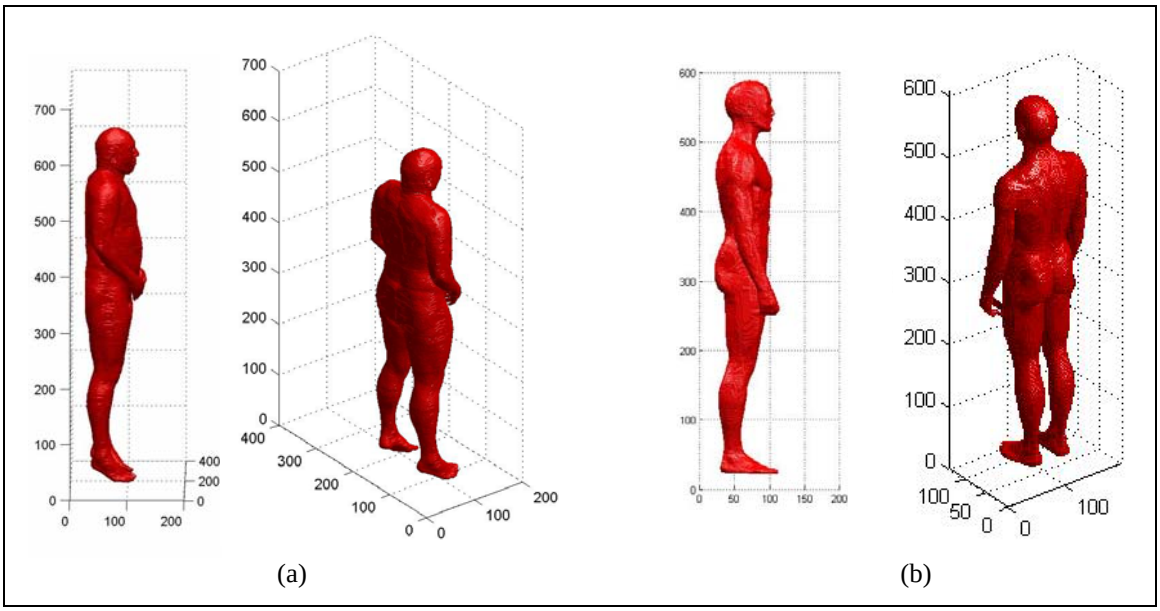

Figure 2. FDTD grid for (a) the fat man body model and (b) the fit man body model.

NOTE: The units on the axes are numbers of FDTD cubic cells with a 3 mm side.

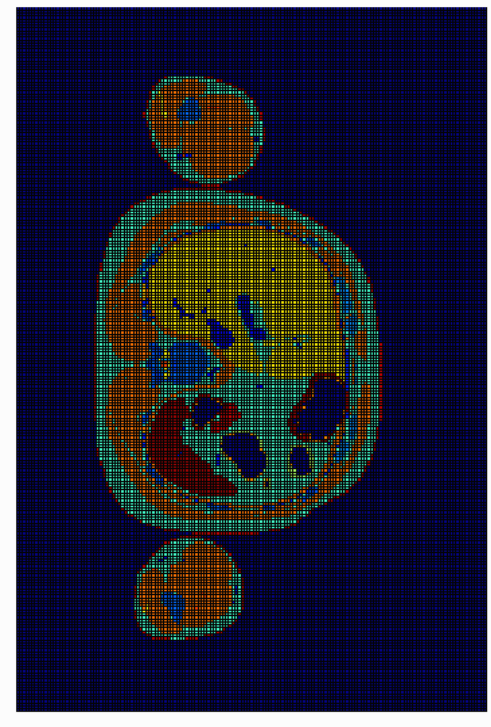

Figure 3. Cross section through the torso of the fat man model.

NOTE: The detailed internal structure of the body tissues is available for this grid. Each different color represents a different tissue type.

The human body meshes in figure 2 were originally obtained for the basic standing position, as shown in the figure. Since we were interested in studying the radar signature of the human body in various postures, we searched for software that allowed articulating the meshes in different positions. For the mesh in figure 2a, we employed a software package called VariPose (produced by Remcom (*13*)). This program allows rearticulating the fat man mesh, including the entire internal organ structure. Examples of rearticulated fat man meshes, obtained with VariPose, are presented in figures 4 and 5. For the mesh in figure 2b, we utilized another software package, called Maya (developed by Autodesk, Inc. (*14*)), which has very powerful and realistic three-dimensional animation capabilities. An example of the rearticulated fit man mesh, obtained with Maya (and other mesh conversion programs), is presented in figure 6.

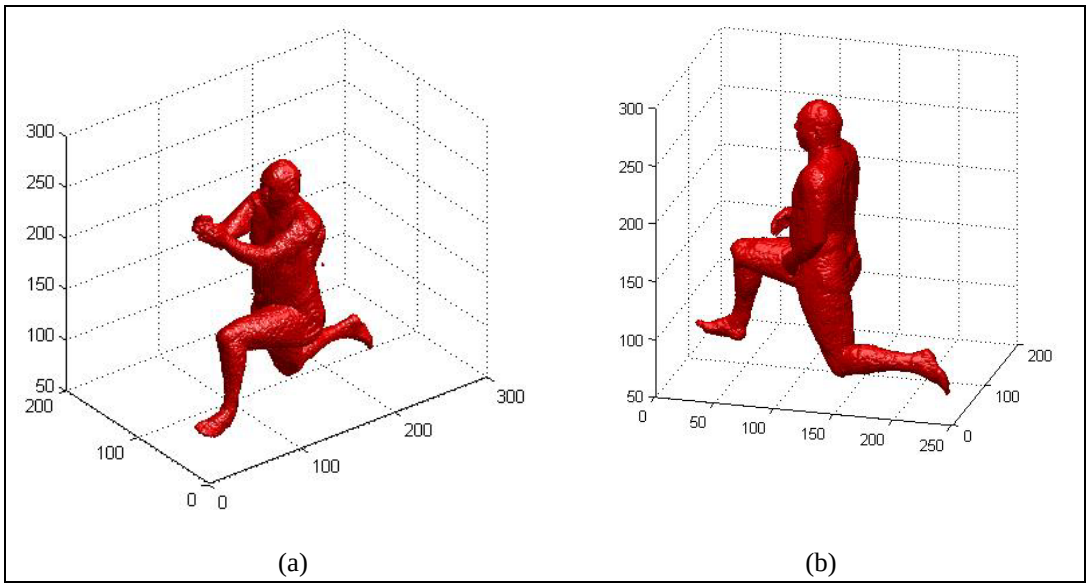

Figure 4. Fat man body model, repositioned in (a) kneeling-shooting and (b) kneeling postures using the VariPose software package to modify this grid.

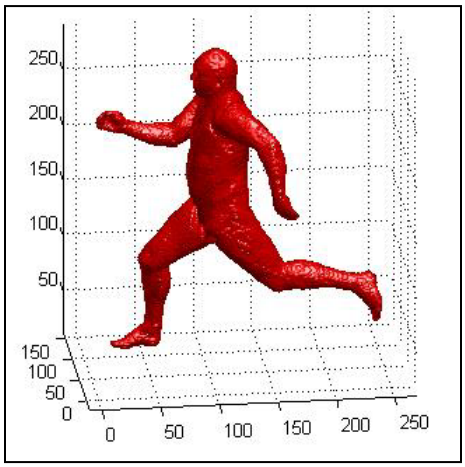

Figure 5. Fat man body model, repositioned in a running posture using the VariPose software package to modify this grid.

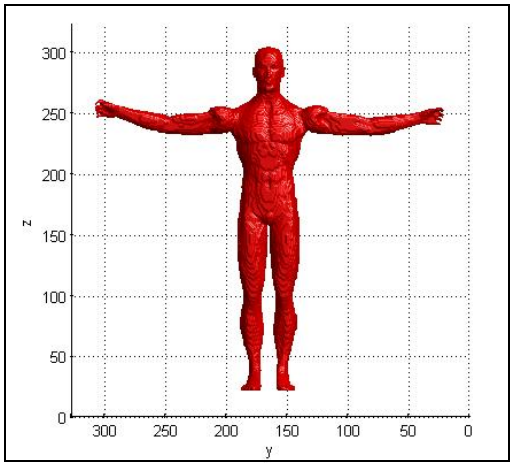

Figure 6. Fit man body model repositioned in a stretched-arms posture using the Maya software package to modify this grid.

3.2 Human Body Radar Cross Section

We computed the RCS (*15*) of the human body in various postures in a wide range of frequencies for all possible azimuth aspect angles and all polarization combinations, using the AFDTD code. Figure 7 shows the human body RCS versus frequency for incidence from the front up to 9 GHz. In this case, we used the fat man mesh (full model) in the standing position (figure 2a) with a cell resolution of 2 mm. Throughout this section, we consider that incidence from the front corresponds to the azimuth angle $\phi = 0°$. Also, unless explicitly specified otherwise, the elevation angle is 0° (propagation vector in the *x*-*y* plane) and the human mesh is placed in free-space. In all cases, we assume a monostatic scenario (the observation is in backscatter). The plots in figure 7 cover both co-polarization combinations, vertical-vertical (V-V) and horizontal-horizontal (H-H). As one can tell from these graphs, there is no major polarization difference for the radar return of the human body in free-space. Also, we notice that, for most frequencies, the RCS of the body as seen from the front varies in a range between -10 and 0 dBsm.

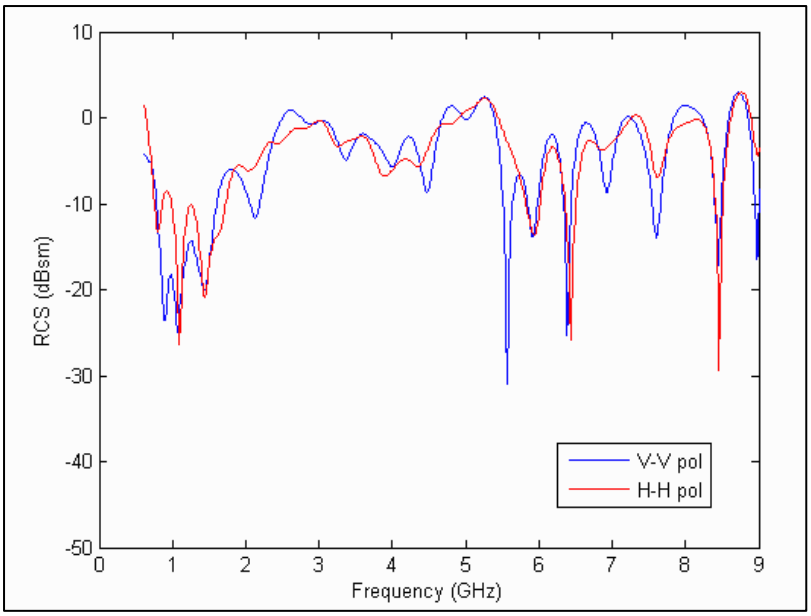

Figure 7. RCS of the human body (fat man model) at 0° azimuth (front view) and 0° elevation in free-space, using a 2 mm resolution FDTD grid.

In figure 8 we tried to address the issue of grid cell resolution necessary for an accurate model up to a certain frequency. It is obvious that a smaller cell size involves a larger computational grid, resulting in increased memory and computing time requirements (for example, going from a 3 mm to a 2 mm grid involves $1.5^3 = 3.4$ times more memory and $1.5^4 = 5$ times more computing time). In figure 8 we compared the RCS obtained on the 3 mm and 2 mm resolution grids. At 1 GHz, the 3 mm cell size results in 100 spatial samples per wavelength in free-space. While this spatial sampling rate is more than sufficient in free-space (*4*), it is not clear whether this is also sufficient inside high-permittivity materials, such as the human muscle with $\varepsilon_r = 54$. However, by looking at the graphs in figure 8, we noticed that the two plots start to diverge significantly only above 5 GHz, meaning that, up to 5 GHz, a grid resolution of 3 mm is satisfactory for our models. Since most of our simulations in this study were limited to frequencies under 5 GHz, we normally utilized the 3 mm human grid (except for the simulations in figures 7, 9 and 10, which go up to 9 GHz and required the 2 mm grid).

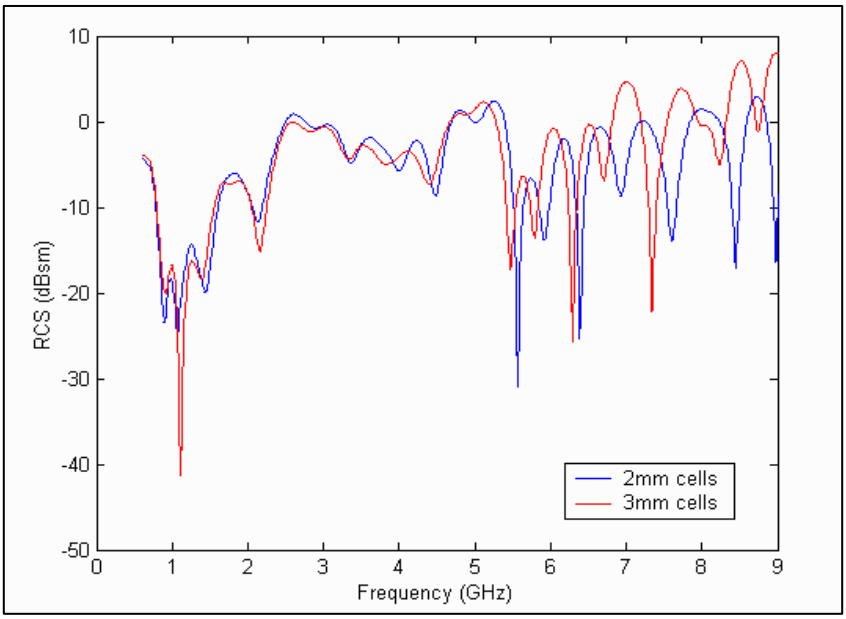

Figure 8. RCS of the human body (fat man model) computed on 2 mm and 3 mm resolution grids, respectively (with a 0° azimuth (front view), 0° elevation, and V-V polarization); the solutions start to diverge around 5 GHz.

Another issue we tried to address was the accuracy of the uniform dielectric model of the human body, as compared to the full model. In figure 9, we compared the RCS of the "real" model to that of a body made of uniform material with dielectric properties close to the skin (V-V polarization, incidence from the front). In both cases, we utilized the same geometrical mesh (the fat man). At $\varepsilon_r = 50$, $\sigma = 1$ S/m, the uniform dielectric material acts almost as a perfect reflector, so penetration in this case should not play a significant role in the radar return. The differences between the two graphs are an indication of how much the penetration of electromagnetic radiation through the human body had an influence on the RCS. Looking at the two graphs, we concluded that, except for low frequencies (up to 1.2 GHz), the penetration through the body is not important in RCS calculations. However, as expected, the lower frequencies do penetrate the skin and hit a relatively low dielectric/loss fat tissue, bouncing back and creating destructive interference.

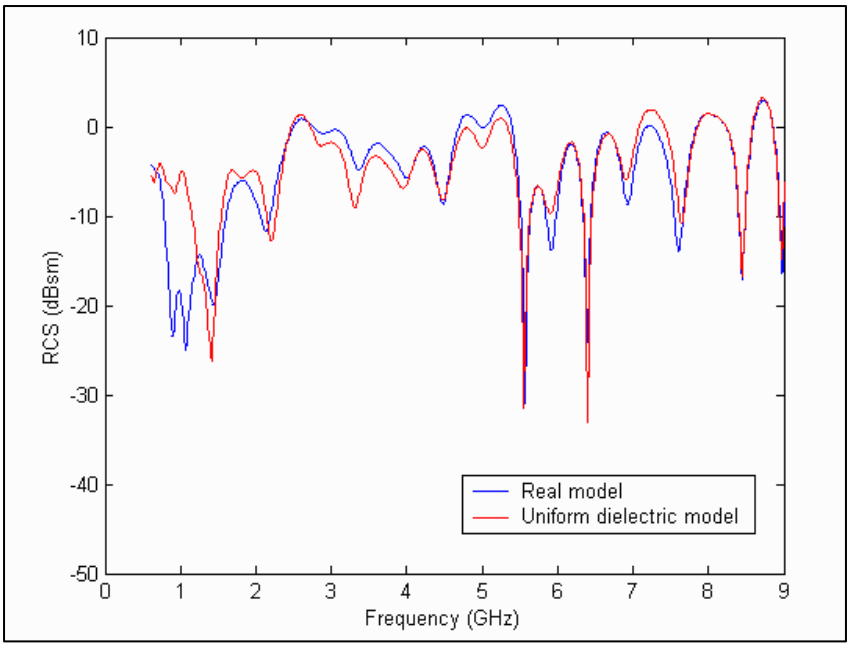

Figure 9. RCS comparison between the complete fat man body model and a body model with identical geometry, but made of a uniform dielectric material (with a 0° azimuth (front view) at 0° elevation and V-V polarization); the differences occur mainly below 1.2 GHz.

In table 1, we give a cell-by-cell list of the tissues along a line going through the middle of the abdomen along the direction of propagation. As one can notice, the fat tissue, which lies immediately behind a thin layer of skin, has a significantly lower dielectric constant and conductivity, allowing further penetration of the low frequency radiation inside the body. It should be stressed that these results were obtained for the particular human body type of the fat man. We can expect that a body with less fat tissue exhibits a smaller difference in RCS between the two models, even at low frequencies. In our subsequent simulations, we use the full model (which is more realistic) whenever possible, however, in some cases (especially for the fit man mesh), we must use the uniform dielectric model. In these situations, we need to keep in mind that we may overestimate the RCS by a few dBs around 1 GHz.

Table 1. Cell-by-cell dielectric properties of the tissues along a line going through the middle of the fat man abdomen, with a computational grid cell size of 3 mm and dielectric constant and conductivity computed at 1 GHz.

Cell Number	Tissue Type	Dielectric Constant	Conductivity (S/m)
1	Skin	40.936180	0.899784E+00
2	Fat	5.447040	0.535018E-01
3	Fat	5.447040	0.535018E-01
4	Fat	5.447040	0.535018E-01
5	Fat	5.447040	0.535018E-01
6	Fat	5.447040	0.535018E-01
7	Fat	5.447040	0.535018E-01
8	Fat	5.447040	0.535018E-01
9	Muscle	54.811050	0.978209E+00
10	Fat	5.447040	0.535018E-01
11	Fat	5.447040	0.535018E-01
12	Fat	5.447040	0.535018E-01
13	Fat	5.447040	0.535018E-01
14	Fat	5.447040	0.535018E-01
15	Fat	5.447040	0.535018E-01
16	Intestine	57.482390	1.127420e+00
17	Mucous membrane	45.711761	8.819710e-01
18	Air	1.000000	0.000000E+00
19	Air	1.000000	0.000000E+00
20	Air	1.000000	0.000000E+00
21	Air	1.000000	0.000000E+00
22	Air	1.000000	0.000000E+00
23	Air	1.000000	0.000000E+00
24	Air	1.000000	0.000000E+00
25	Air	1.000000	0.000000E+00
26	Air	1.000000	0.000000E+00
27	Air	1.000000	0.000000E+00
28	Intestine	57.482390	1.127420e+00
29	Fat	5.447040	0.535018E-01
30	Fat	5.447040	0.535018E-01
31	Fat	5.447040	0.535018E-01
32	Fat	5.447040	0.535018E-01
33	Fat	5.447040	0.535018E-01
34	Fat	5.447040	0.535018E-01
35	Fat	5.447040	0.535018E-01
36	Fat	5.447040	0.535018E-01

NOTE: The cells are numbered from the front towards the back, and the cell list is not complete—it stops somewhere in the middle of the abdomen.

With regard to the frequency-independent dielectric constant and conductivity limitation of the AFDTD code mentioned in section 3.1, we ran a simple test to evaluate its impact on our models. First, we utilized the permittivity and conductivity computed at 1 GHz (from the original data in (*11*)), then we ran the same simulation again with the material properties computed at 3 GHz. The results are shown in figure 10 and clearly prove that, except around 1 GHz, there is no difference between the two calculations. This is consistent with the conclusion in the previous paragraph, since the reflection coefficient of the skin is not expected to vary much with frequency. However, the differences around 1 GHz (where we have some penetration through the body) suggest that using frequency-independent ε and σ, equal to the values computed at 1 GHz, is acceptable over a wide band of frequencies.

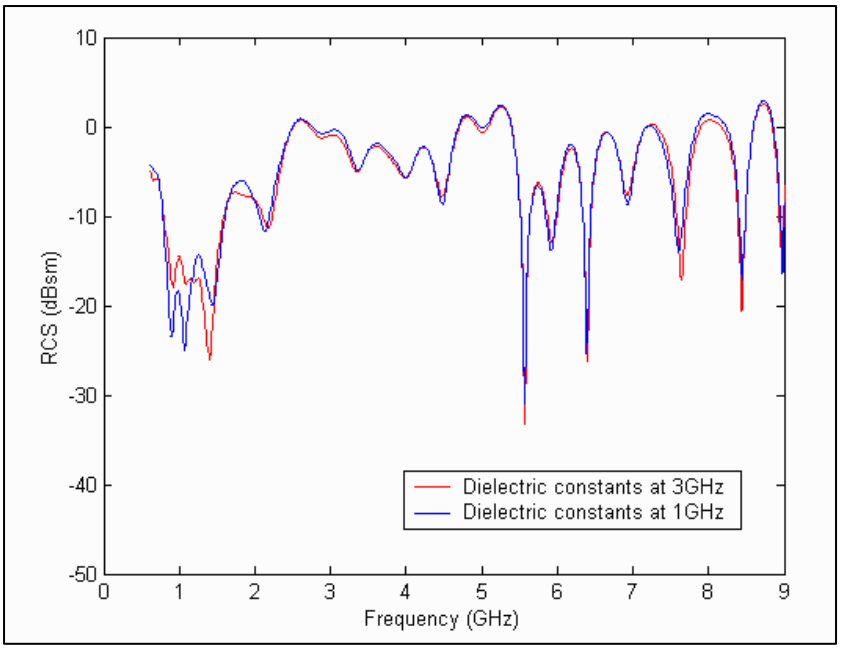

Figure 10. RCS of the human body (fat man model) with a dielectric constant of tissues computed at two different frequencies (with a 0° azimuth (front view), 0° elevation, and V-V polarization); the differences are negligible, except at low frequencies (around 1 GHz).

We also tried to validate the human body models based on our AFDTD code against other independent CEM codes. Although many CEM techniques cannot easily handle materials with very high permittivity and loss, such as many of the human body tissues, we managed to obtain RCS data for the fit man mesh, generated by the Time-Domain Electro-Magnetic Parallel Unstructured Simulator (TEMPUS) program (courtesy of Dr. V. Shankar of Hypercomp, Inc. (*16*)). TEMPUS is a Finite-Volume Time-Domain code, which employs techniques borrowed from computational fluid dynamics, and operates in the time domain on a highly unstructured mesh. In figure 11, we compare the fit man RCS obtained with AFDTD and TEMPUS in the 0.5 to 3 GHz range for incidence at 0° elevation and 0° azimuth in both polarizations. In the FDTD model, we used a uniform dielectric mesh with $\varepsilon_r = 50$, $\sigma = 1$ S/m; however, for the TEMPUS

model, we set the imaginary part of the permittivity constant (frequency-independent) at $\varepsilon'' = 18$, while keeping the real part $\varepsilon' = 50$. Despite this difference between the two models, the agreement in the computed RCS is very good.

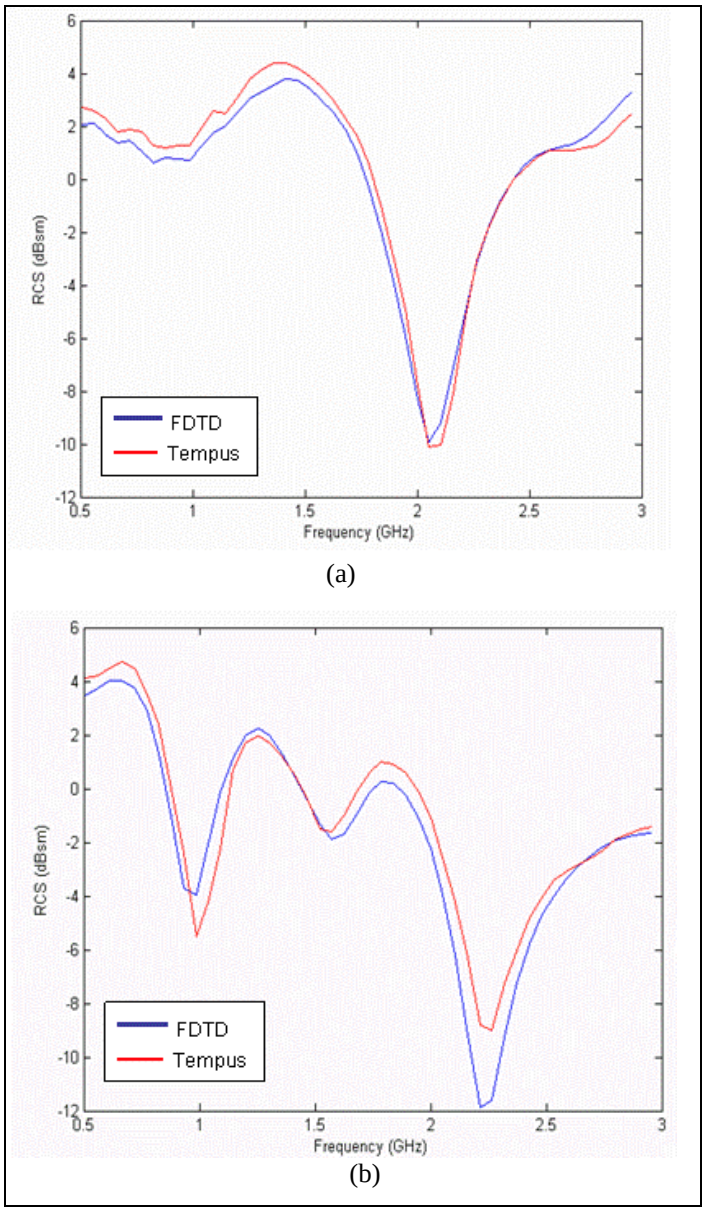

Figure 11. RCS of the fit man body model as computed by ARL's FDTD code and Hypercomp's TEMPUS code, with a 0° azimuth (front view) and 0° elevation, showing (a) V-V and (b) H-H polarization.

NOTE: The TEMPUS data courtesy of Dr. V. Shankar of Hypercomp, Inc.

Next, we study the human body RCS variation with the azimuth aspect angle at a given frequency. Figure 12a and 12b plot the RCS of the "fat man" in the standing (figure 2a) and the kneeling-shooting (figure 4a) positions, respectively, for azimuth angles ranging from 0° to 360°, around 1 GHz. In order to make these calculations more representative for a UWB radar, we actually plotted the average RCS obtained for frequencies ranging from 0.8 GHz to 1.2 GHz (400 MHz bandwidth). The effect of this averaging procedure is to smooth out some of the fast angular variation of the RCS at one particular frequency. We plotted the same kind of graphs for these two positions, this time around 2 GHz, in figure 13a and 13b. One immediate conclusion is that the kneeling posture (figure 4a) produces more interesting RCS variation than the standing position (figure 2a), since there is a larger number of scattering centers in the former case. A persistent feature (that can be noticed for all positions) is the strong return from the back (ϕ = 180°). That can be explained by the fact that this body model's back is mostly flat, creating a larger RCS as compared to the more curved surfaces characteristic to other parts of the body. As expected, the angular RCS variation becomes more rapid as we increase the frequency. However, on the average, we notice similar RCS levels around 1 and 2 GHz.

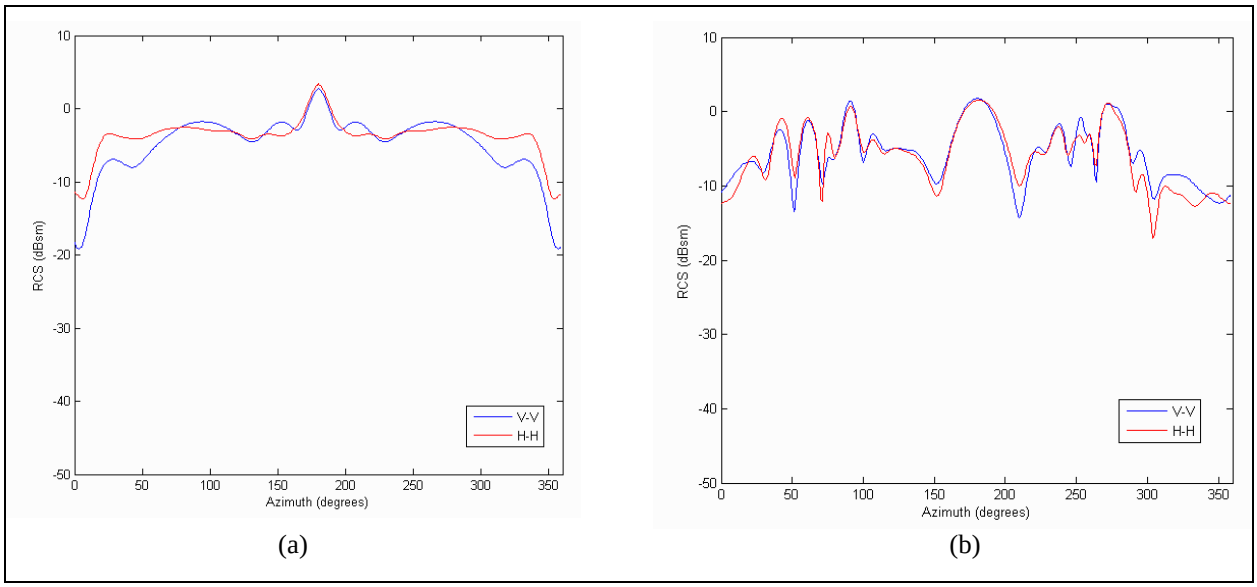

Figure 12. RCS of the standing human (fat man model from figure 2a) body (a) and RCS of the kneeling human (fat man model from figure 4a) body (b) versus azimuth angle at 0° elevation in free-space, where the average RCS was computed over a 400 MHz band centered at 1 GHz.

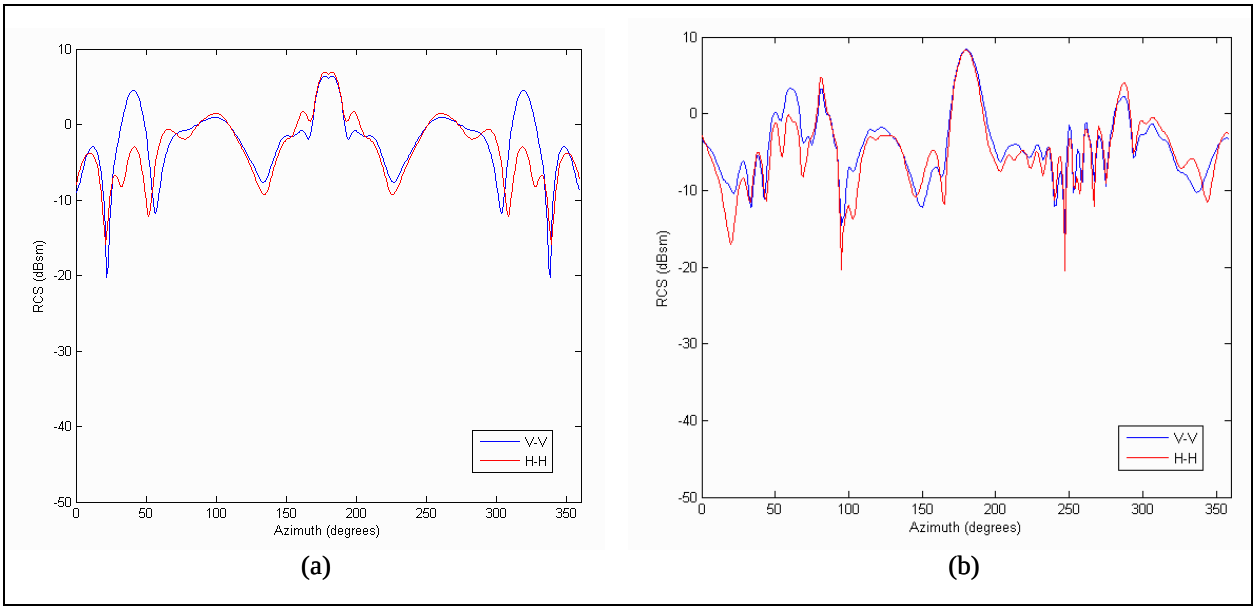

Figure 13. RCS of the standing human (fat man model from figure 2a) body (a) and the kneeling human (fat man model from figure 4a) body (b) versus azimuth angle at 0° elevation in free-space, where the average RCS was computed over a 400 MHz band centered at 2 GHz.

Another problem of interest is investigating the statistics of the human body RCS, as the azimuth angle is varied. By plotting histograms of the RCS versus angle, we were able to evaluate the shape of the RCS probability distribution functions. We found that these distributions conform reasonably well to the classic Swerling models (*17*). In general, at low frequencies, the distribution approaches Swerling Case 3 distribution, given by the expression

$$p(\sigma) = \frac{4\sigma}{\sigma_a^2} \exp\left(-\frac{2\sigma}{\sigma_a}\right), \tag{1}$$

where σ is the RCS and σ_a the average RCS. At high enough frequencies, we are closer to the Swerling Case 1 distribution, given by the expression

$$p(\sigma) = \frac{1}{\sigma_a} \exp\left(-\frac{\sigma}{\sigma_a}\right). \tag{2}$$

The frequency where we notice a transition from one model to the other varies with the body position, but in general is somewhere between 1 and 2 GHz. In figures 14 and 15, we present a few RCS histograms at specific frequencies, and the matching probability distribution functions (renormalized to the total number of samples). From these plots we concluded that, for the kneeling man, the transition from Case 3 to Case 1 takes place at a frequency lower than for the standing man (notice that the standing man still matches Case 3 at 1.8 GHz).

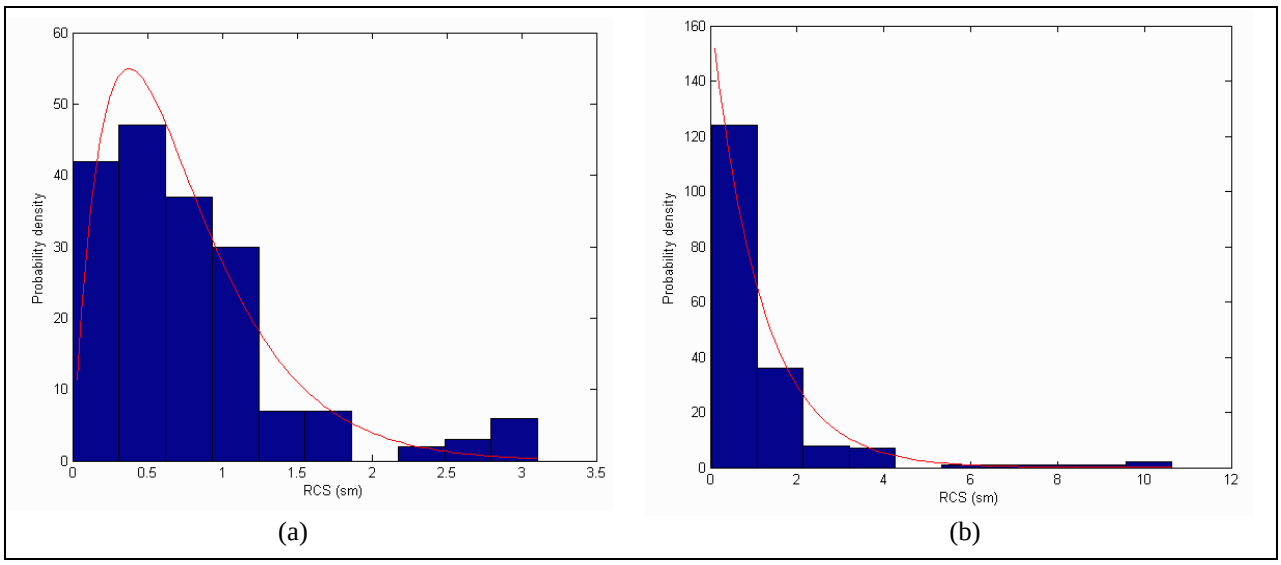

Figure 14. Probability distribution function of the standing human body RCS (fat man model in figure 2a), as the azimuth angle is varied at 0° elevation in free-space with V-V polarization, showing the RCS at (a) 1.8 GHz versus Swerling Case 3 model and (b) 2.5 GHz versus Swerling Case 1 model.

NOTE: The blue bars show a histogram of the computed data, and the red line shows a renormalized probability distribution function according to Swerling models.

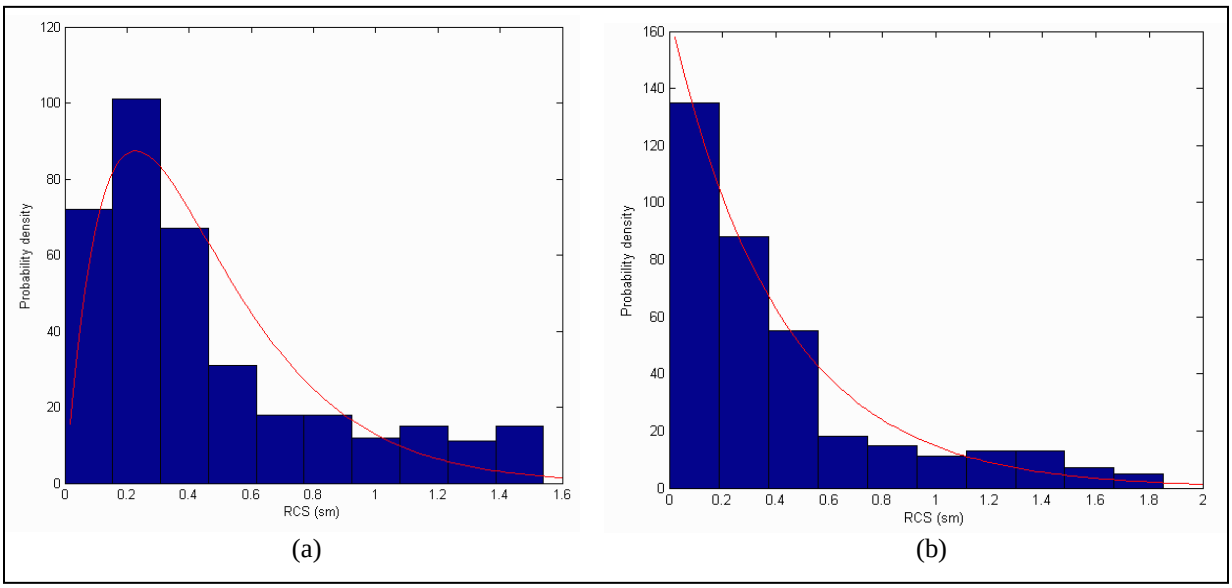

Figure 15. Probability distribution function of the kneeling human body RCS (fat man model in figure 4a), as the azimuth angle is varied at 0° elevation in free-space with V-V polarization, showing the RCS at (a) 0.5 GHz versus Swerling Case 3 model and (b) 1 GHz versus Swerling Case 1 model.

NOTE: The blue bars show a histogram of the computed data and the red line shows a renormalized probability distribution function according to Swerling models.

We also proceeded to plotting the average RCS versus frequency for different body postures (the average RCS is computed over all azimuth angles from 0° to 360°). This average RCS represents the expected return from a human body when its orientation with respect to the radar is not known *a priori* (as it should always be the case for a human behind a wall). Some of these results are summarized in figure 16. In that figure, (a) and (b) represent the average RCS of the fat man in standing and kneeling-shooting postures, respectively, whereas (c) and (d) represent the average RCS of the fit man in standing (figure 2b) and spread-arm (figure 6) postures, respectively. The striking thing that we notice in these plots is that the average human body RCS remains in a very tight range (between -4 and 0 dBsm) for all frequencies and all body positions. This is a result that holds in a wide range of frequencies, at least up to X-band.

The RCS differences that we notice in the lower part of the spectrum (between 0.5 and 1.5 GHz), between the fat man and the fit man charts, are caused by the fact that we use different dielectric models for the two meshes (full model versus uniform dielectric model, as explained in a previous paragraph). One explanation for the average RCS being independent on the body position is that the main contribution to the radar return comes from the trunk. As long as this one stays in upright position, the relative position of the limbs cannot modify the average return in a significant amount. Moreover, as the results presented here show, the body shape does not have a major influence on the average RCS. However, we expect the human body RCS to be much more dependent on the overall body size. These findings are useful in the context of a target recognition pre-screening process, where the magnitude of the radar return can be utilized to reject targets that do not fall between the limits characteristic to the human body.

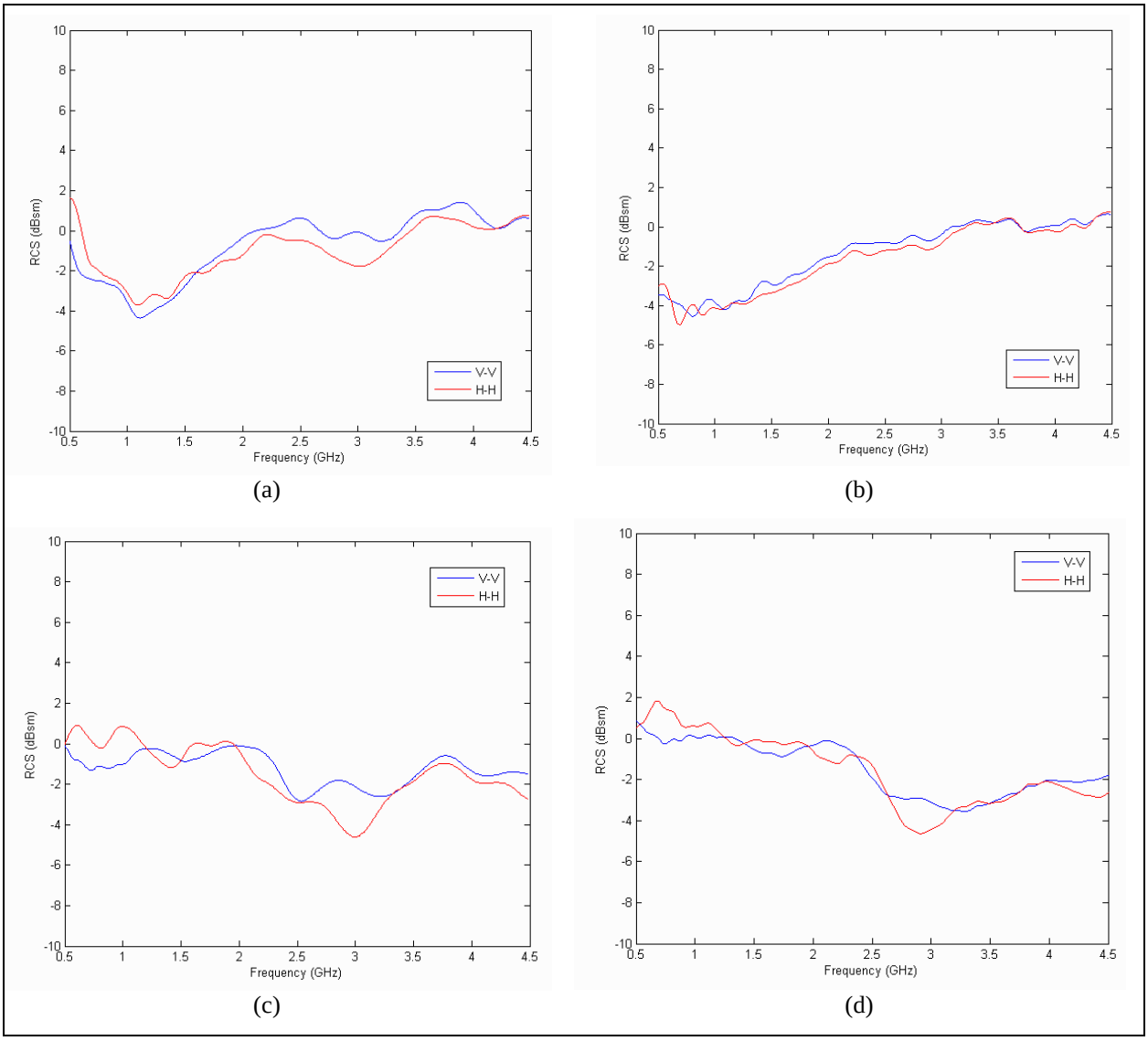

Figure 16. Mean RCS (averaged over all azimuth angles versus frequency at 0° elevation in free-space) of a (a) standing fat man body (from figure 2a), (b) kneeling fat man body (from figure 4a), (c) standing human fit man body (figure 2b; unlike the fat man, this model is made of a uniform dielectric material), and (d) fit man with stretched arms (from figure 6).

The incidence at 0° elevation is characteristic for a ground-based radar scenario (such as hand-held or vehicle-mounted). For an airborne radar scenario, we need to consider higher elevation angles. In this case, we added an infinite dielectric ground plane (ε_r = 10, σ = 0.05 S/m), for a more realistic model. Figures 17 through 18 compare the human body RCS computed in free-space and over a dielectric ground plane at various elevation angles at 1 GHz for V-V and H-H polarization, respectively. The calculations here were made on the fat man mesh in the standing position. As expected, the addition of a ground plane has a different impact on the two polarizations, when compared to the free-space RCS. Thus, for shallow elevation angles (15° and 30°), which are close to the Brewster angle (*18*), the ground reflection is very weak in V-V polarization; therefore, there is not much difference between the free-space and the ground plane RCS in this case. The situation is different for H-H polarization, where we see a significant

increase in the RCS level at all elevation angles, when we add the ground plane. As expected, the RCS for V-V polarization increases as well for steeper incidence angle (45° and 60°), when the ground bounce becomes more prominent. Another interesting aspect is the large increase in the RCS of the human body as seen from the back ($\phi = 180°$) for H-H polarization in the ground plane scenario. In this situation, the flat back of the fat man and the ground plane form an almost perfect corner reflector, resulting in large RCS at any elevation incidence angle (*15*).

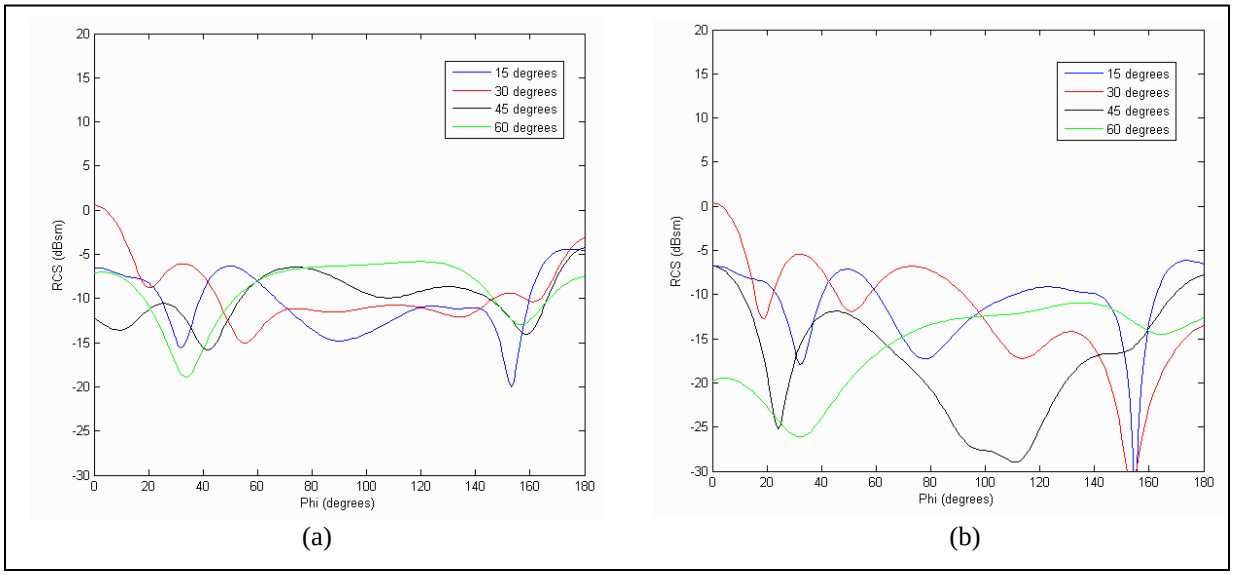

Figure 17. RCS of a standing human (fat man from figure 2a) over a dielectric ground plane (a) and in free-space (b) at 1 GHz with V-V polarization, where the angle on the abscissa is the azimuth and the angle in the legend is the elevation.

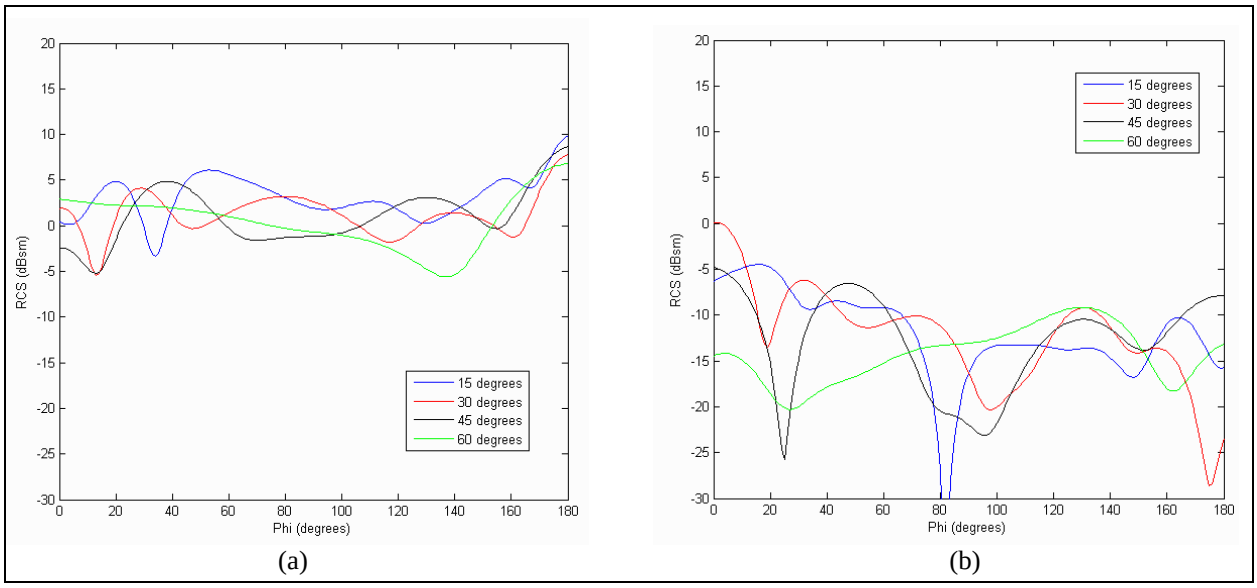

Figure 18. RCS of a standing human (fat man from figure 2a) over (a) a dielectric ground plane and (b) in free-space at 1 GHz with H-H polarization, where the angle on the abscissa is the azimuth and the angle in the legend is the elevation.

3.3 Synthetic Aperture Radar Images of the Human Body

So far, we looked at the human body RCS for specific frequencies and incidence angles, as modeled by the FDTD method. Another problem of interest for the radar engineers is obtaining SAR images based on the computer simulations. Here, we consider UWB pulse excitation, which is ideally suited for FDTD simulations, since this algorithm operates directly in the time domain. In forming a SAR image, we use the bipolar time-domain response of the target, obtained for a certain range of incidence angles, and use the back projection algorithm (*19*). The time-domain response to a UWB incident pulse at one aspect angle can be obtained with the FDTD method in only one run; however, we need separate FDTD runs in order to obtain the responses at different incidence angles. In this section, our SAR image formation algorithm assumes a side-looking operation mode (*19*), with the radar moving on a straight path perpendicular to the direction of propagation in the middle of the synthetic aperture. Since our FDTD code produces results for a far-field scenario, with plane wave excitation and the radar moving on a circle around the target (the distance radar-target is constant), we must first process the FDTD output data to reflect the side-looking radar operational mode.

The difference between the two scenarios is illustrated in figure 19. The fields at the receiver computed by FDTD do not include the $1/R$ term (characteristic for the spherical wave decay in the far-field (*18*)); therefore, the standoff distance between radar and target does not matter (as long as it is consistent with the far-field assumption). Moreover, when computing the SAR image intensity (in dB), we do not include the $1/R$ term either (this can always be adjusted in post-processing), making the image independent of the standoff distance as well. One possible inconsistency between our model and a real side-looking SAR system is that we consider all aspect angles in the aperture to contribute with equal weights. Consequently, we do not take into account the real radar antenna pattern, but assume that, at each point on the synthetic aperture, the antenna radiates equally in all directions. However, this is not necessarily a bad assumption given the fact that, at low frequencies, the antenna beamwidth of a side-looking SAR system is usually large, typically reaching values between 60° and 90°. In some cases, we introduce a Hanning (raised cosine) window (*20*) taper as the antenna pattern, making it a more realistic scenario. However, this procedure decreases the image cross-range resolution, while at the same time reducing the sidelobes.

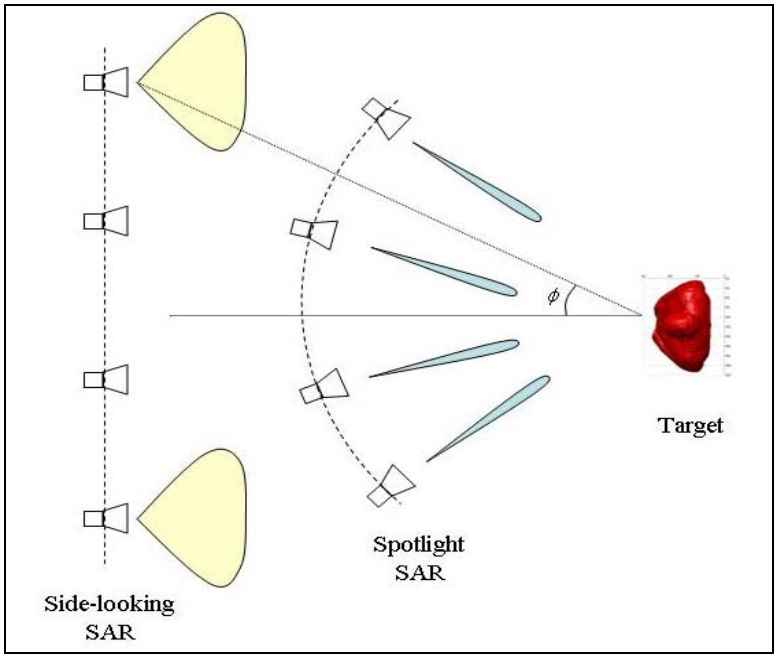

Figure 19. Geometry of the SAR image formation process, showing the conversion from spotlight SAR mode (electromagnetic model data) to side-looking SAR mode (image data).

NOTE: The spotlight mode operates with plane waves at specific incidence angles. The side-looking mode operates with wide beam antenna patterns (in most cases, we use omni-directional patterns).

Although the FDTD excitation pulse spectrum did not matter in the RCS computations (as long as it covered the frequency range of interest), this becomes important when feeding the time-domain data into the SAR image formation algorithm. In this section, we typically used the pulse in figure 20, called the 4th order Rayleigh pulse (*21*). This is a very convenient waveform for FDTD simulations, because it has a small duration, and, at the same time, a clearly limited spectrum. Moreover, it has no direct current (DC) component. If f_c is the center frequency of the pulse, then the 6 dB bandwidth extends from about $0.5f_c$ to $2f_c$. (It should be noted that using the term "center frequency" in this context is inaccurate, since the pulse spectrum is asymmetric with respect to its peak, and f_c actually designates the peak frequency.) This interval of about $1.5f_c$ can be utilized as an effective bandwidth when evaluating the downrange resolution of the SAR image (for a definition of the effective pulse bandwidth, see reference *22*). The image resolution is given by the following equations:

$$\Delta y = \frac{c}{2BW} \tag{3}$$

$$\Delta x = \frac{R\lambda}{2L}, \tag{4}$$

where Δy is the downrange resolution, Δx is the cross-range resolution, c is the speed of light, BW represents the effective bandwidth of the pulse, R is the range from aperture to target, λ is the wavelength at the center frequency, and L is the synthetic aperture length. It is important to mention that, in all the SAR images presented throughout this report, the pixel size is much smaller than the resolution as computed by equations 3 and 4 (the images look "smooth"). This is achieved by very fine two-dimensional interpolation of the image intensity map. Nevertheless, this interpolation process does not add any information that would allow the separation of distinct image features.

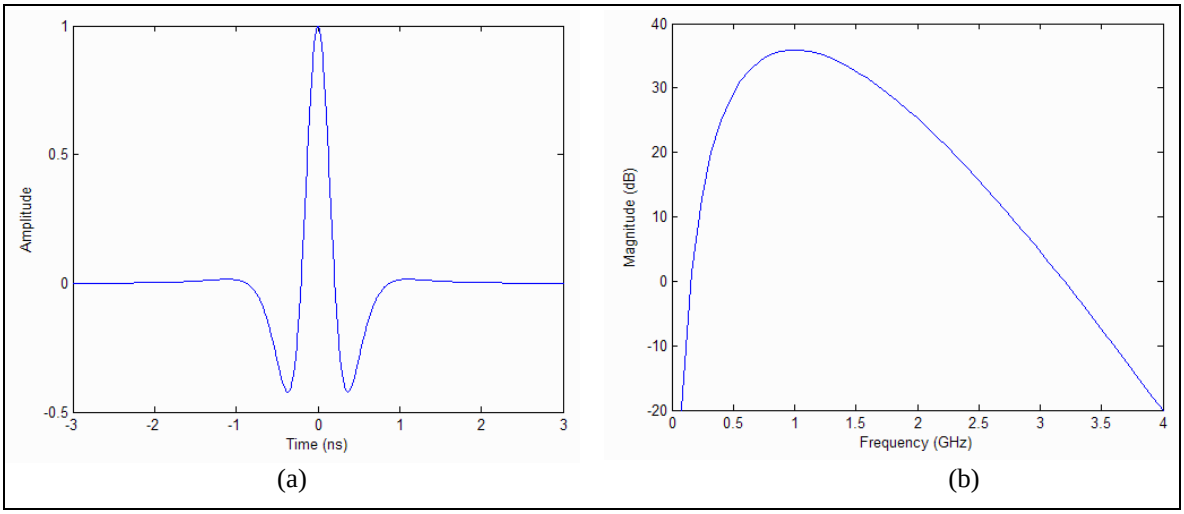

Figure 20. Typical UWB excitation pulse (Rayleigh 4th order) used in the SAR images in this study, showing (a) the pulse in the time domain and (b) the pulse spectrum; in this case, the pulse spectrum peaks at 1 GHz and has a 6 dB bandwidth extending from approximately 0.5 to 2 GHz.

Figure 21 represents the SAR images obtained for the fat man in the standing position. In these images, as well as the subsequent ones, we assume propagation in free-space with a 0° elevation.

NOTE: In all the SAR figures (figures 21–23, 25–27, 30, 33, and 34), the images represent top views of the man as he looks down the page. The radar moves on a path parallel to the x axis and looks up from the bottom of the page (in the center of the synthetic aperture, the radar is pointed at the front of the man). The down-range is along the y axis, whereas the cross-range is along the x axis. The units on the axes are in meters. The pixel intensities (in dB) are mapped into a pseudocolor scale. In all cases displayed here, the angular aperture is 40°.

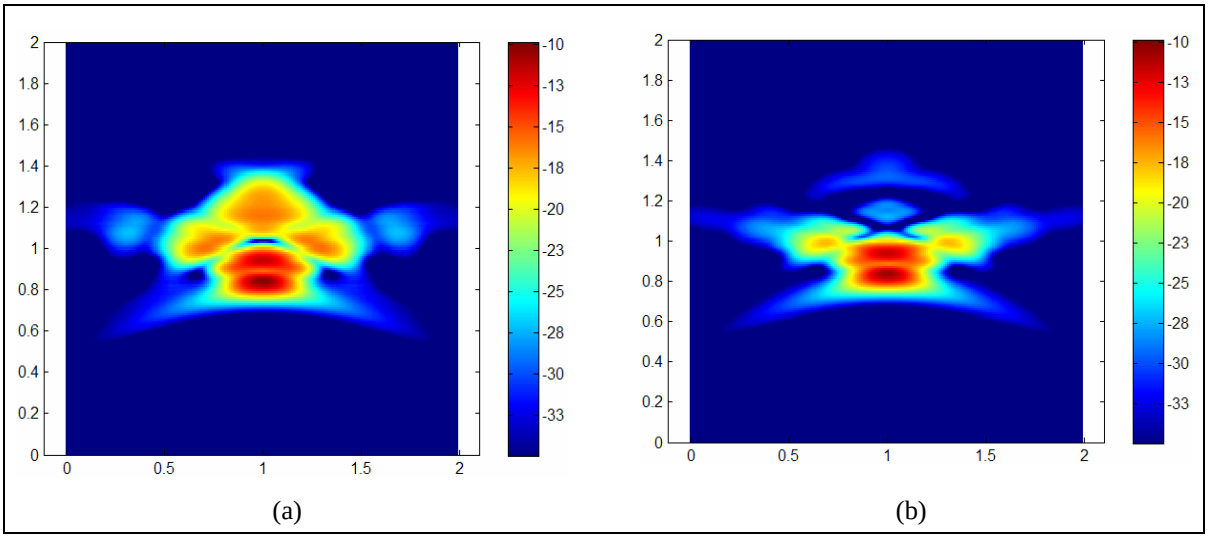

Figure 21. SAR image of a standing human (fat man from figure 2a) in free-space at 1 GHz center frequency, 1.5 GHz bandwidth, and 40° integration angle with (a) H-H and (b) V-V polarization.

One major feature that we identify in the SAR images is the front of the man, shown as the brightest spot in the middle of image. In order to identify other scattering centers, we removed certain body parts from the original mesh. After removing the arms, we obtained the image in figure 22a. Comparing the images in figures 21a and 22a, we concluded, as expected, that the arms and shoulders contribute with the bright spots on the sides (in the full model). More complicated was attempting to explain the late-time return, which appears in the middle of image, above the main return, in figure 21. When we removed the legs, we noticed that the late-time return almost disappeared (compare figures 21a and 22b). A more detailed analysis showed that the late-time return is the effect of double bouncing of the incident wave off the legs, with a significant return in the backscatter direction.

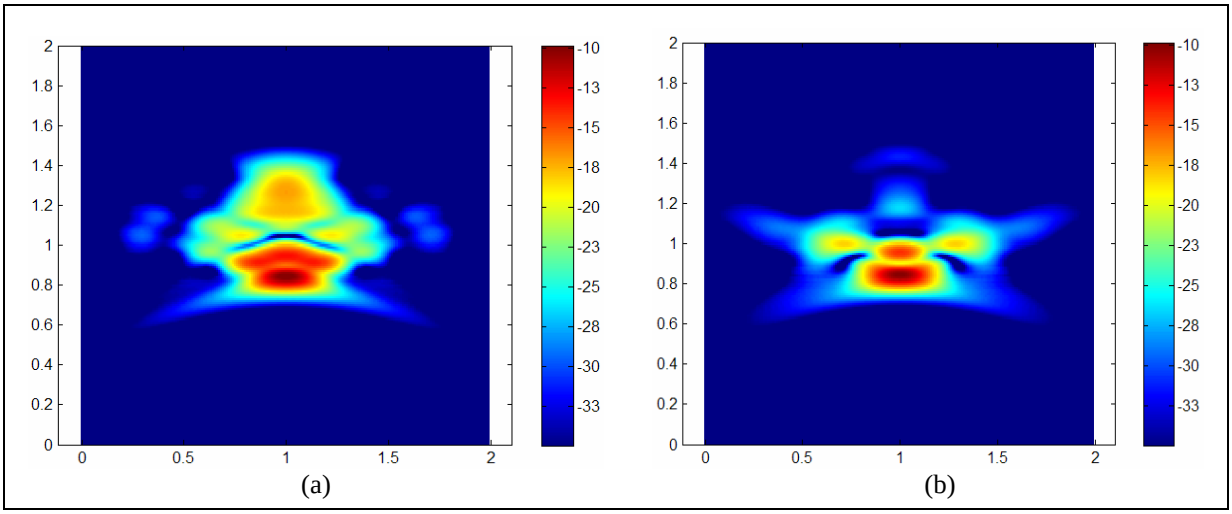

Figure 22. SAR images of modified human body models—(a) human body mesh without arms and (b) human body mesh without legs—in free-space at 1 GHz center frequency, 1.5 GHz bandwidth, 40° integration angle, and H-H polarization.

In order to explain the double bouncing off the legs effect and its impact on the SAR image of the human, we studied a simplified version of it, namely we created the SAR images of two parallel vertical metallic cylinders of 20 cm diameter and 50 cm height for various separation distances between the cylinders. In these simulations, the center frequency is 2 GHz, the bandwidth 3 GHz, and the angular aperture 40°. In figure 23 we show the SAR images obtained when the cylinders are placed 20 cm and 40 cm apart, respectively. Simple geometric considerations allow us to calculate the downrange displacement *D* between the late-time return and the direct bounce off the front of the cylinders, for normal incidence:

$$D = \frac{a}{2} + 2R\left(1 - \frac{\sqrt{2}}{2}\right) \cong 0.5a + 0.6R\,, \tag{5}$$

where *R* is the cylinder radius and *a* is the distance between cylinders, as shown in figure 24. By looking at the SAR images in figure 23, we obtain displacements *D* of about 17 cm and 30 cm, which match very well the values calculated by equation 5. It also turns out that, for a limited range of azimuth angles, these double-bounced backscatter rays arrive at the receiver with small phase differences (red and blue rays in figure 24), adding up constructively in the images. The late-time bright spot in the images in figure 23 differs from the late-time feature in figure 21 by the fact that the former is much more localized than the latter. This is the effect of all double bounce contributions along the height of the cylinders arriving with the exact same phase at the receiver (the case in figure 23). At the same time, the human legs have variable diameter along their height, therefore, the double bounce ray paths at different heights may arrive at the receiver with different phases. In consequence, the late-time features in the images in figure 21 appear more diffuse.

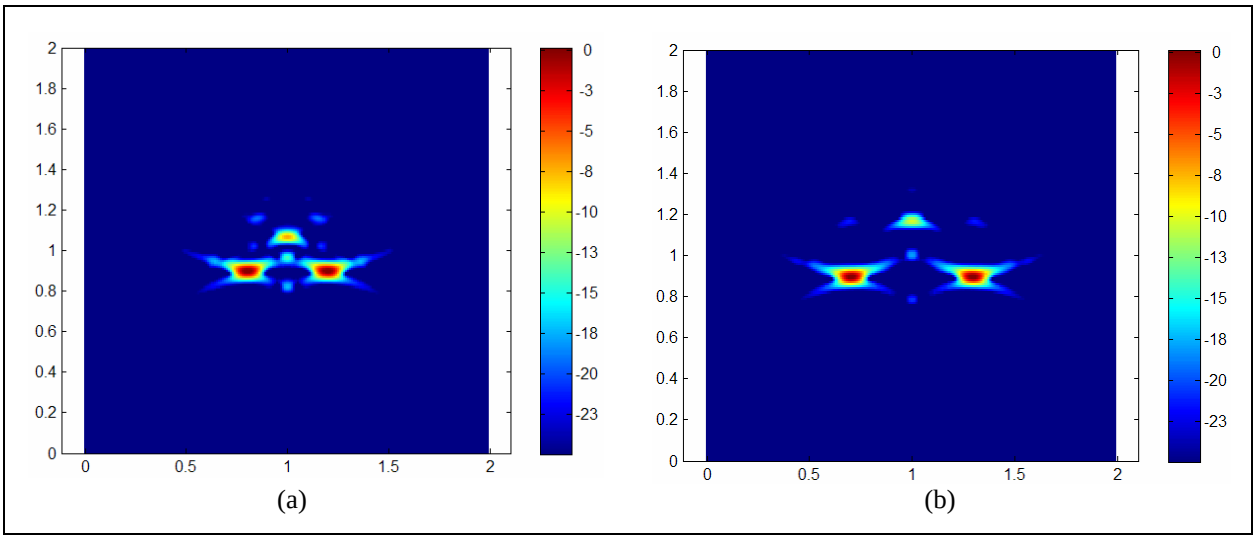

Figure 23. SAR images of two vertical metallic cylinders (0.2 m diameter and 0.5 m height) with (a) a 20 cm separation between cylinders and (b) a 40 cm separation between cylinders placed in free-space with a 2 GHz center frequency, 3 GHz bandwidth, 40° integration angle, 0° elevation, and H-H polarization

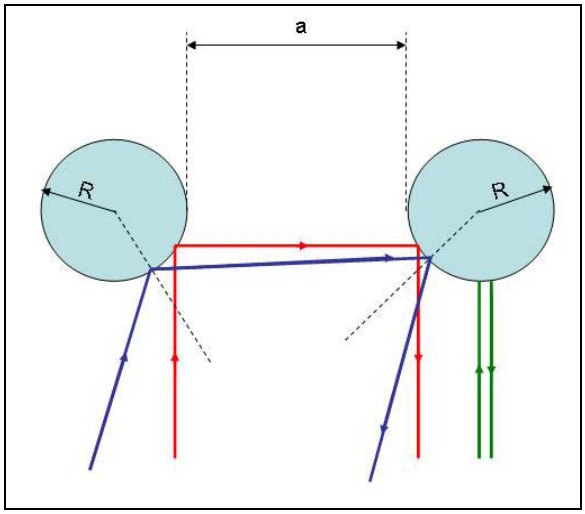

Figure 24. Schematic representation of the double scattering mechanism for the two vertical cylinders in figure 23 (top view).

NOTE: The green arrows indicate the single-bounce ray path from the cylinders and the red and blue arrows indicate two possible double-bounce ray paths. The difference between the red and green path lengths is given by equation 5. For small off-broadside incidence angles, the red and blue rays are almost in phase.

In figures 25 and 26 we image the human in the same posture as in figure 21, but we increase the center frequency to 2 GHz and 3 GHz, respectively. At the same time, we keep a constant bandwidth-to-center-frequency ratio of 1.5. The image resolution increases with the center frequency and bandwidth, ranging from 10 by 10 cm (same in down and cross-range) for 1 GHz,

to 3.3 by 3.3 cm for 3 GHz. These higher frequency images display a finer localization of the scattering centers; however, it is not obvious that they convey any extra information that would facilitate the human target discrimination based on these images alone.

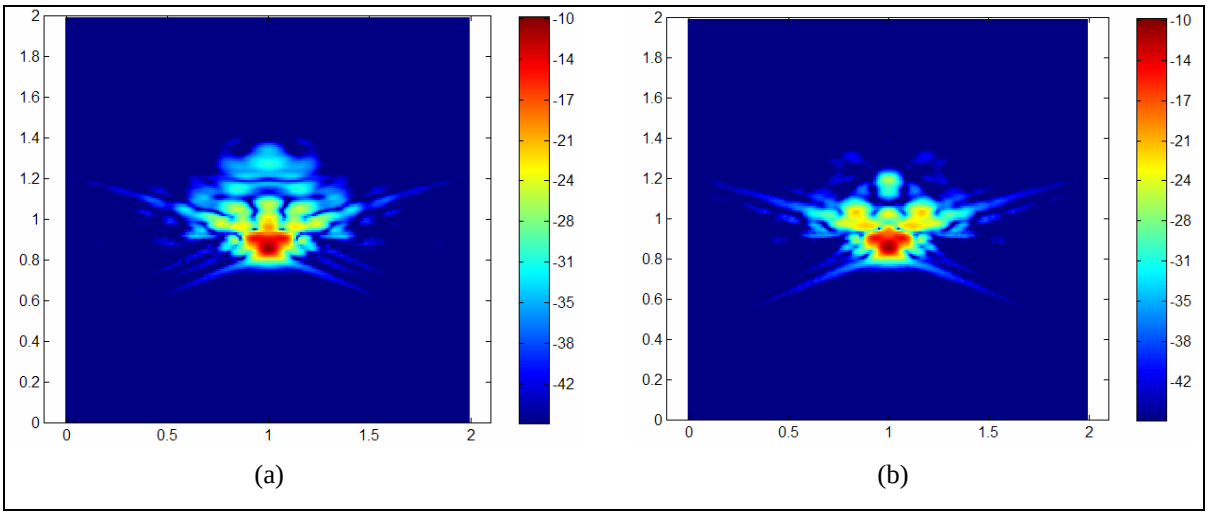

Figure 25. SAR image of a standing human (fat man from figure 2a) in free-space at a 2 GHz center frequency, 3 GHz bandwidth, and 40° integration angle with (a) H-H and (b) V-V polarization.

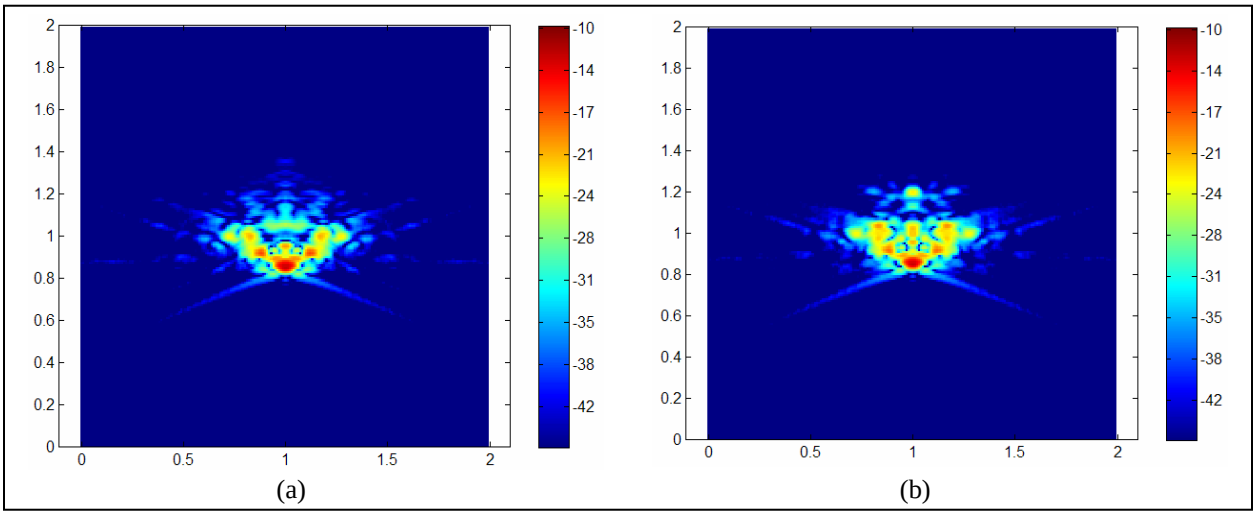

Figure 26. SAR image of a standing human (fat man from figure 2a) in free-space at a 3 GHz center frequency, 4.5 GHz bandwidth, and 40° integration angle with (a) H-H and (b) V-V polarization.

In figure 27, we present the same type of images for the kneeling fat man (figure 4b). The center frequency is 1 GHz and the bandwidth is 1.5 GHz with the other parameters being identical with the previous scenario. We can distinguish more features in this image as compared to figure 21, in particular the front leg (brighter in V-V polarization), and the back foot. However, looking at the image in figure 27 without any *a priori* knowledge, it is difficult to imagine that it represents

a kneeling man. If the man were placed in a highly cluttered environment, such as a room containing furniture, the features that we see in the clean, free-space environment would be more difficult to distinguish.

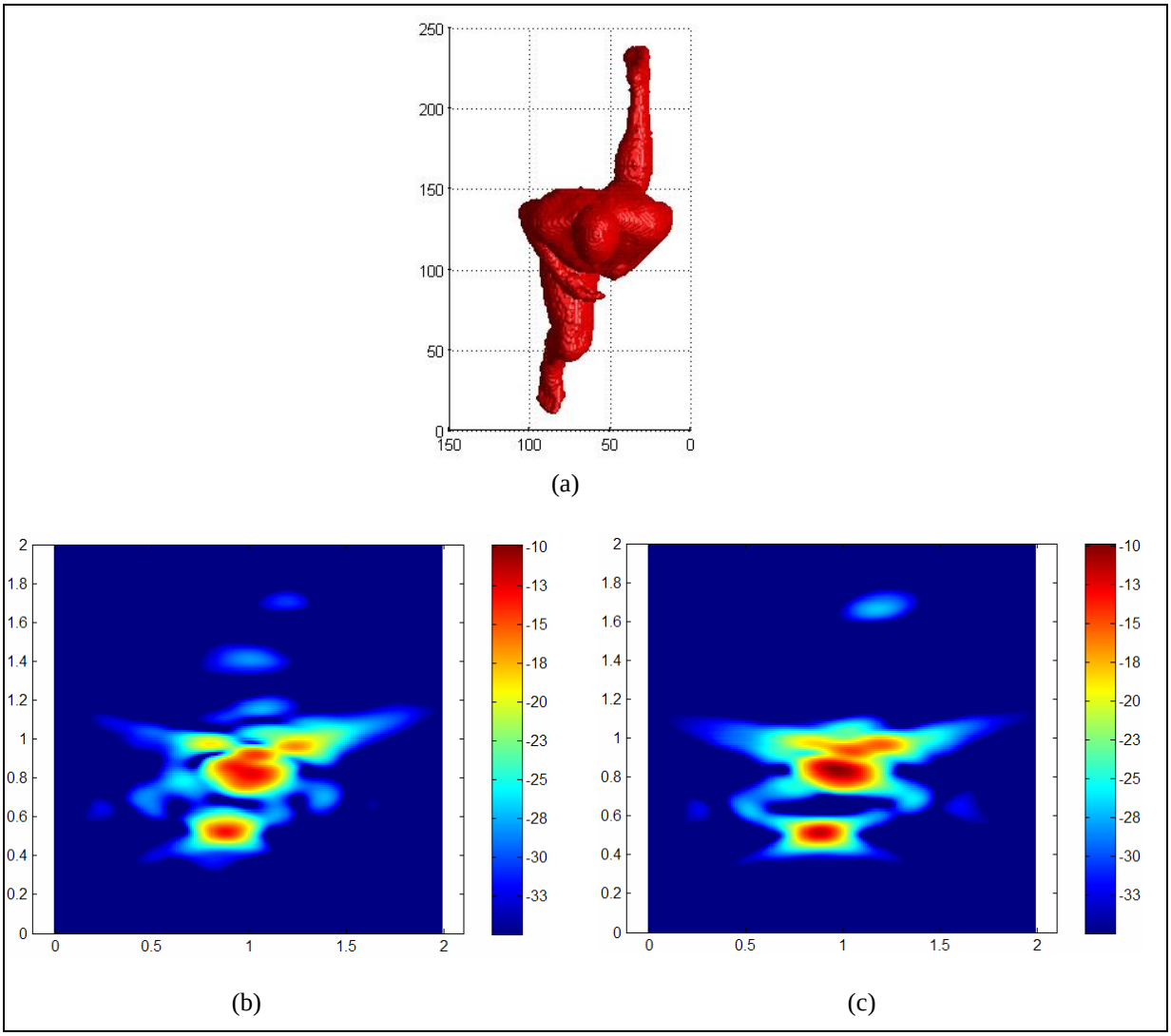

Figure 27. SAR image of a kneeling human (fat man from figure 5b) in free-space at a 1 GHz center frequency, 1.5 GHz bandwidth, and 40° integration angle, showing the (a) top view of the human mesh (as laid out in the SAR image), the SAR image for (b) H-H and (c) V-V polarization.

We continue our study by presenting the changes in the human body RCS and SAR images in a case when the man carries an object resembling a weapon. As a simplified version, the man is equipped with a metallic stick held in vertical position (figures 28 through 30) or tilted at an angle (figures 31 through 33). The metallic stick has a length of 1 m and a diameter of 1.8 cm. It is interesting to notice the strong polarization dependence of the radar return for these scenarios. Figure 29 indicates a significant increase in the RCS for V-V polarization in the 0.5 to 3 GHz frequency range for the man holding the vertical stick (see figure 7 for comparison).

However, the H-H signature does not change much, compared to the plain human body. This can also be seen in the SAR images (figure 30). The stick location appears as a bright spot in the V-V polarized image, indicated by the pink dot in figure 30b (see figure 21b for comparison).

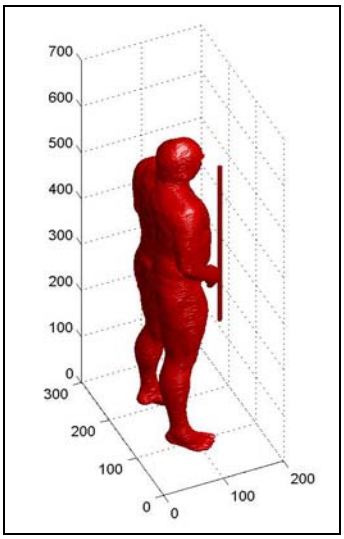

Figure 28. FDTD grid for the fat man holding a vertical metallic stick with a length of 1 m and a diameter of 1.8 cm at a grid resolution of 3 mm.

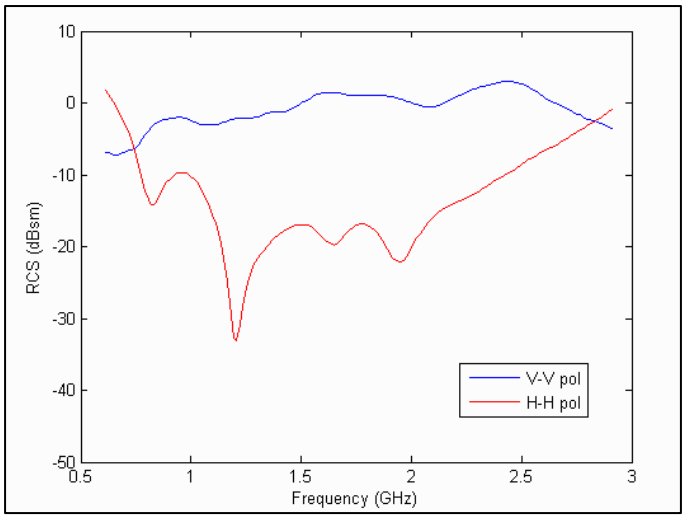

Figure 29. RCS of the standing human holding a vertical metallic stick (as shown in figure 28) at 0° azimuth (front view) and 0° elevation in free-space.

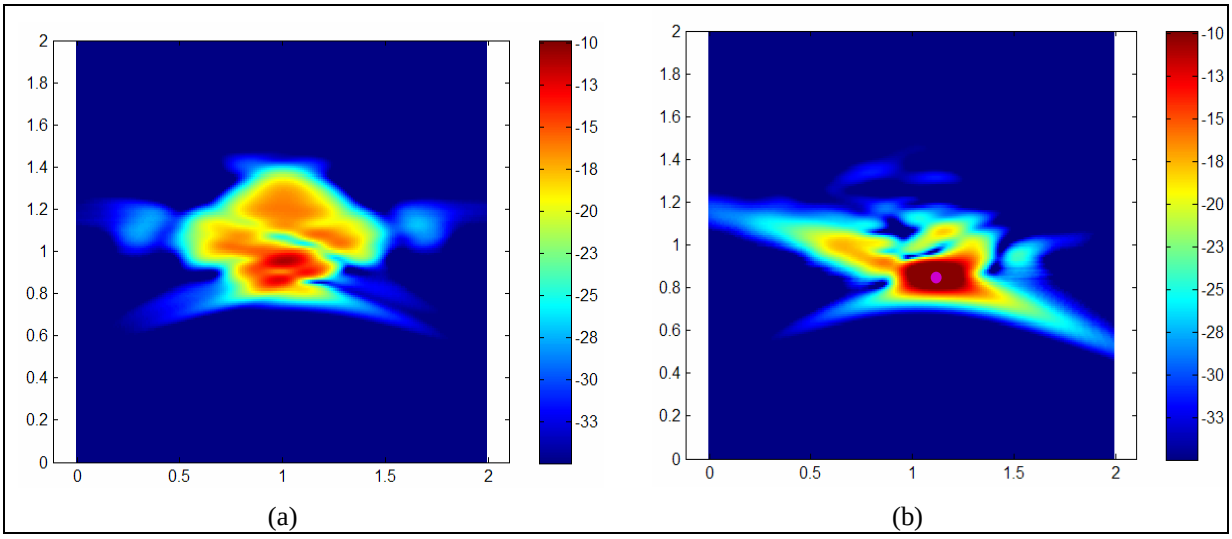

Figure 30. SAR image of a standing human holding a vertical metallic stick (as shown in figure 28) at a 1 GHz center frequency, 1.5 GHz bandwidth, and 40° integration angle with (a) H-H and (b) V-V polarization; the pink dot indicates the stick location.

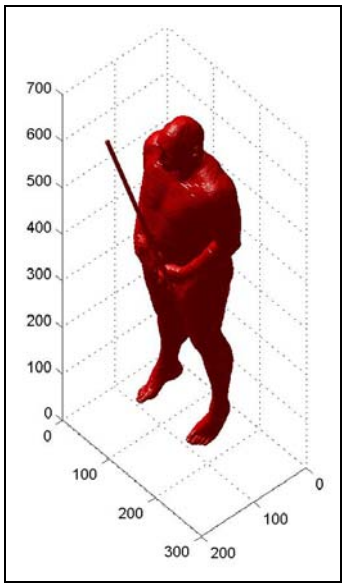

Figure 31. FDTD grid for the fat man holding a tilted (35° with respect to the vertical) metallic stick with a length of 1 m and a diameter of 1.8 cm at a grid resolution of 3 mm.

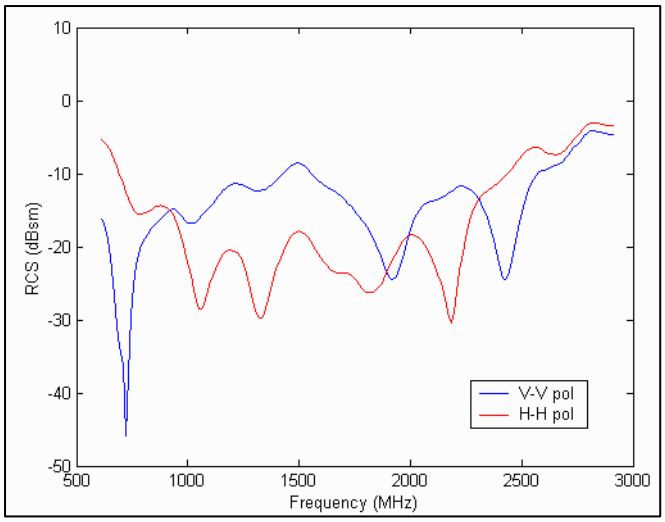

Figure 32. RCS of the standing human holding a tilted metallic stick (as shown in figure 31) at 0° azimuth (front view) and 0^0 elevation in free-space

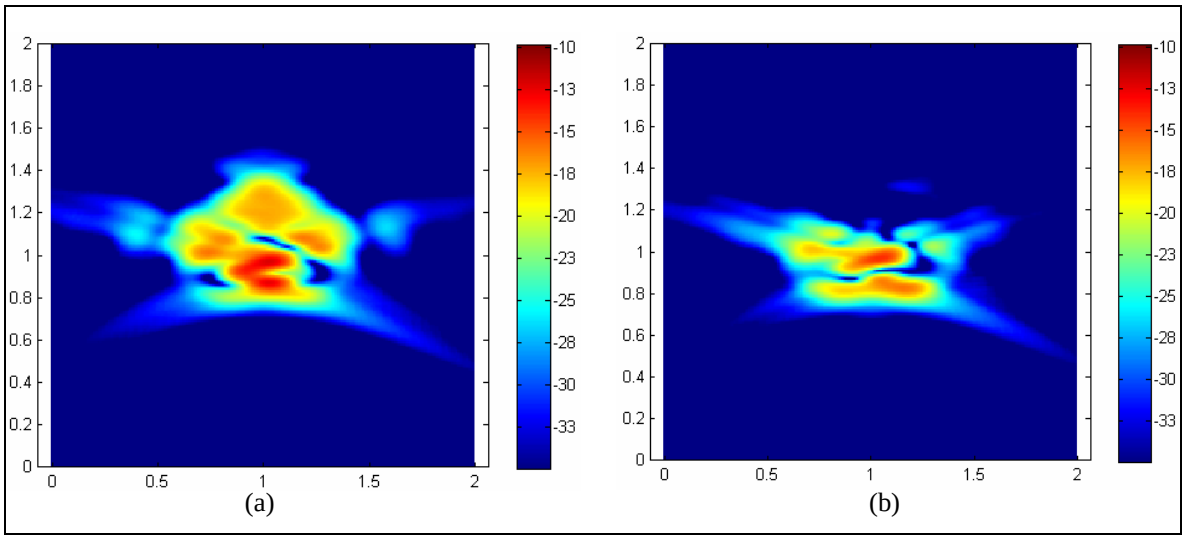

Figure 33. SAR image of a standing human holding a tilted metallic stick (as shown in figure 39) at a 1 GHz center frequency, 1.5 GHz bandwidth, and 40° integration angle with (a) H-H and (b) V-V polarization.

The tilted stick does not have a well-defined effect on the two co-polarization combinations, as evidenced by figures 32 and 33. However, we expect it to have a much larger impact on the cross-polarization radar return. Indeed, if we compare the cross-polarized SAR images in figure 34, we notice a much brighter spot at the stick location for the tilted stick than for the vertical stick (which, basically, has almost no effect on the cross-polarized image). It should be noted that, in general, the cross-polarization radar return is much weaker than in co-polarization (the intensity scale in figure 34 is 10 dB below the scale in the previous images). Nevertheless, our

point here was to demonstrate the impact of the tilted stick on the cross-polarized image as compared to the other scenarios. These examples suggest the fact that a fully polarimetric radar may enhance the chances of discriminating a human carrying a weapon.

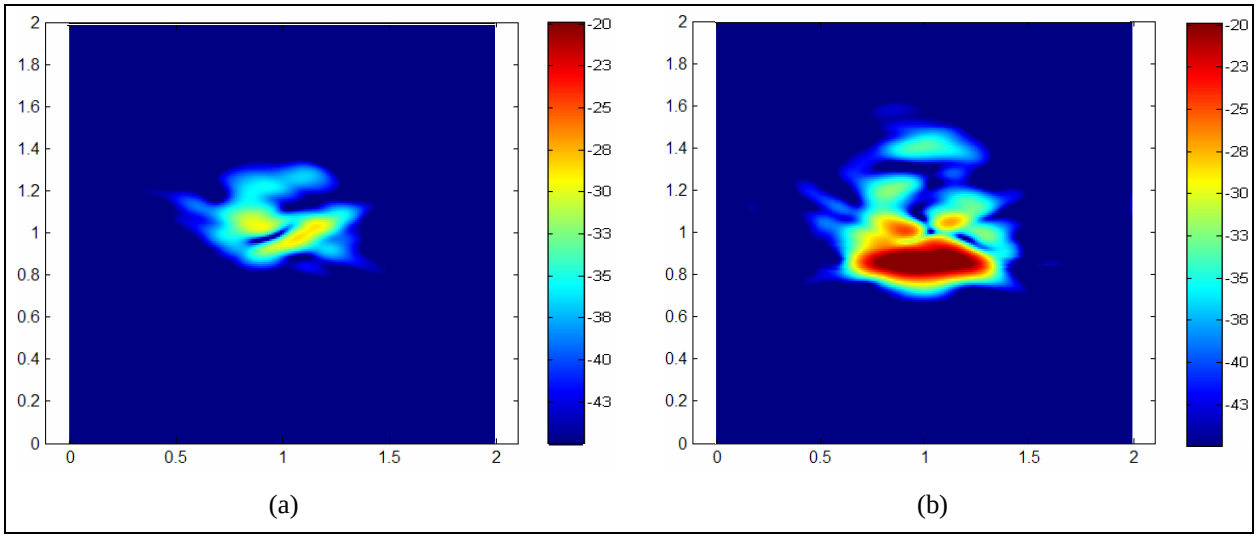

Figure 34. Cross-polarization (V-H) SAR image of a standing human holding metallic stick in different orientations, (a) vertical stick and (b) tilted stick, at a 1 GHz center frequency, 1.5 GHz bandwidth, and 40° integration angle.

3.4 Radar Signature of a Human Behind a Wall

So far, we have analyzed the radar signature of a human placed in free-space or eventually above a ground plane. For STTW applications, we need to investigate how this signature changes when the human is placed behind a wall, as shown in figure 35. In this section, we indicate ways of computing such signature. We first mention that the FDTD code does not allow for the inclusion of an infinite wall in the computational domain, because of problems in the vicinity of the boundaries (which must be free-space). Also, including a single finite length wall in front of the human has drawbacks, because of the strong scattering from the wall's edges, which can actually be stronger than the return from the human. Thus, the only way to actually compute the through-wall signature of a human is to place him in a full four-wall room (including a ceiling and a floor) and separate the human contribution from the overall backscatter return from the room. In fact, placing the human in a complete room creates a more realistic model of the STTW scenario than considering just a human behind a single wall.

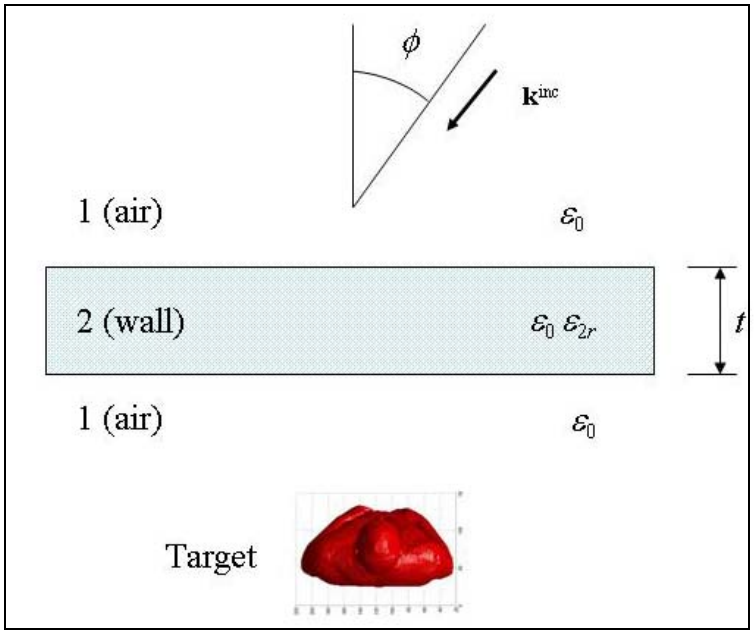

Figure 35. Computing the RCS of a human placed behind a wall, where a plane wave is incident at an azimuth angle ϕ on the wall and the wall is considered homogeneous with complex relative permittivity ε_{2r} and thickness t.

A representation of the modeling setup is shown in figure 36, where the fit man is placed in the middle of a 5 m by 3.5 m by 2.2 m room, with 12 in. thick brick walls and 6 in. thick concrete slabs for ceiling and floor. The ceiling and floor are necessary in order to avoid edge diffraction of the incident plane wave from the back of the front wall and the front of the back wall (it should be mentioned that these are FDTD modeling artifacts, and they would not be encountered in a real radar system, utilizing an antenna in the near-field). The dielectric properties are $\varepsilon_r = 2.3$, $\sigma = 0.03$ S/m for bricks and $\varepsilon_r = 6.8$, $\sigma = 0.1$ S/m for concrete. We looked at the range profiles that were obtained at 0° elevation and 0° azimuth for a pulse excitation centered at 2.5 GHz with a 2 GHz effective bandwidth. As opposed to the previous section, this time we synthesized the pulse in the frequency domain, by utilizing a Hanning spectral window (*20*), as shown in figure 37. The FDTD grid has a 5 mm cell resolution.

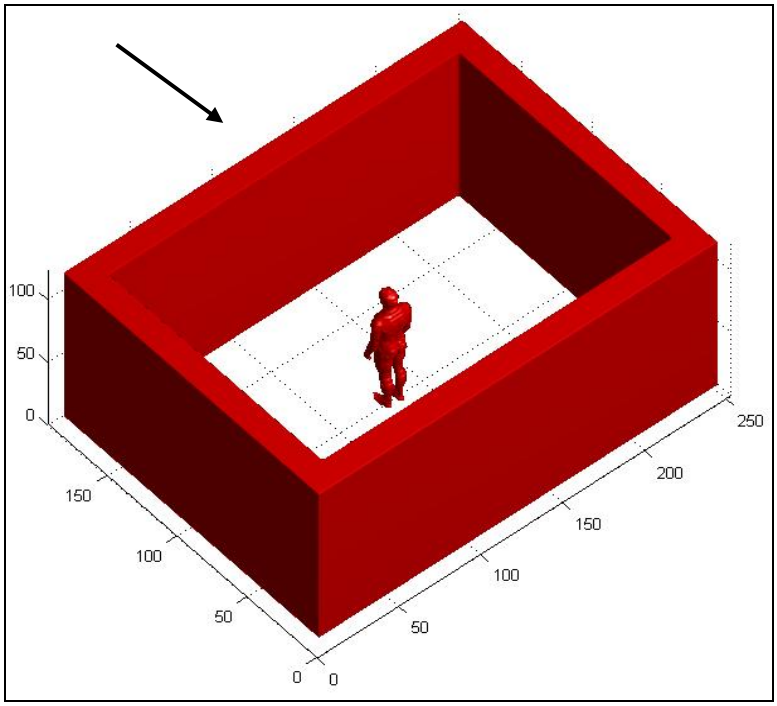

Figure 36. The geometry of the models utilized in calculating the RCS of a man inside a 5 m by 3.5 m by 2.2 m room with 12 in. thick walls made of bricks, and 6 in. thick concrete slabs covering the bottom and the top; in this case, the fit man (figure 2b) has been placed in the middle of the room.

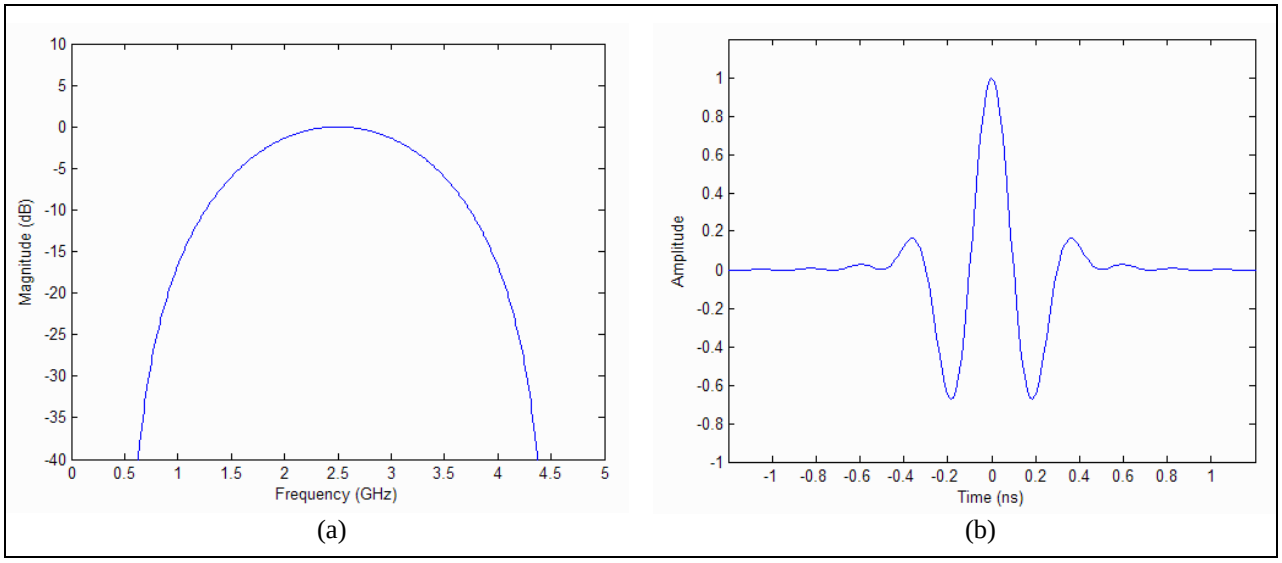

Figure 37. UWB pulse defined by a Hanning frequency window with the center frequency at 2.5 GHz, showing (a) the pulse spectrum and (b) the pulse in the time domain; the total bandwidth extends from 0.5 to 4.5 GHz, and the effective bandwidth is only 2 GHz around the center frequency.

Figure 38 presents the range profiles that were obtained from the FDTD models, when the man was present (red line) or absent (light blue line) from the room. In green, we show an overlay of the front and back wall, as well as the human mesh, all seen from the top. We notice that, for

most part, the two lines (red and blue) overlap, except for a section corresponding to the contribution of the human. In fact, the difference between the two range profiles constitutes the signature of the human behind a wall.

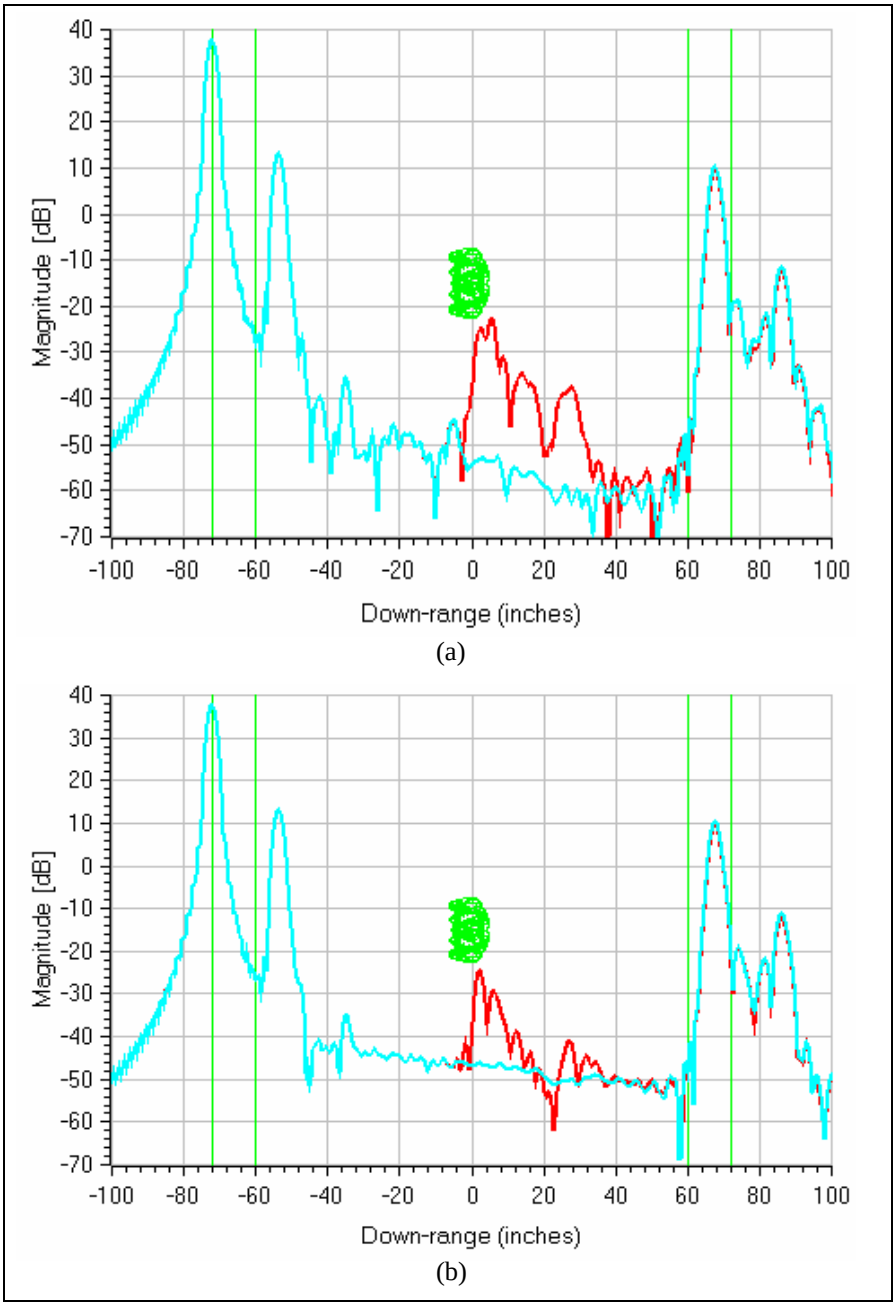

Figure 38. Range profiles of a human body in a brick wall room, as described in figure 36, with a 0° azimuth, 0° elevation, 2.5 GHz center frequency, and 2 GHz effective bandwidth showing (a) V-V and (b) H-H polarization.

NOTE: The light blue line represents the range profile of an empty room, whereas the red line includes the man in the room. The green lines outline a top view of the room (front and back wall), as well as the human body mesh in the middle.

However, for an infinite homogeneous wall, one can imagine a more direct way to compute the RCS of a human behind the wall, by simply adding an analytic correction to the human free-space RCS, that accounts for a roundtrip transmission through that wall. This correction is given by the following "transfer function":

$$T = \left(\frac{T_{12} T_{21} \exp\left(- jk_0 t \left(\frac{\varepsilon_{2r}}{\sqrt{\varepsilon_{2r} - \sin^2 \phi}} - \frac{1}{\cos \phi} \right) \right)}{1 - R_{12} R_{21} \exp\left(-2 jk_0 t \sqrt{\varepsilon_{2r} - \sin^2 \phi} \right)} \right)^2 , \qquad (6)$$

where R_{12}, R_{21}, T_{12}, T_{21} are the reflection and transmission coefficients from medium 1 (air) to medium 2 (wall material) and vice versa, respectively (*18*); t is the wall thickness; k_0 is the propagation constant in free space; ε_{2r} is the complex relative permittivity of the wall material; and ϕ is the azimuth angle of propagation. Although this model is simple, its main advantage is that, computationally, it is orders of magnitude faster than the "in room" technique presented above.

We tested the validity of these two approaches by comparing the resulting RCS of the fit man placed behind a brick wall. Figure 39 compares the "in room" and the "analytic" RCS obtained at $\phi = 0°$, for V-V and H-H polarizations, respectively. The free-space RCS was also added to the charts for comparison. We notice that the match between the two methods is satisfactory, apart from a few ripples that appear in the "in room" plots, due to the higher complexity of that scenario. The match is still good if we consider off-broadside incidence, as in figure 40 (where $\phi = 30°$). Finally, we present the case of a cinder block wall, where an analytic formulation of the wall transmission and reflection is not available (since the cinder block is not a uniform medium). In that case, we must utilize the "in room" approach to compute the RCS of the human behind the wall. The results are shown in figure 41, where we also included for comparison the RCS of the human behind the brick wall, as well as the free-space human RCS.

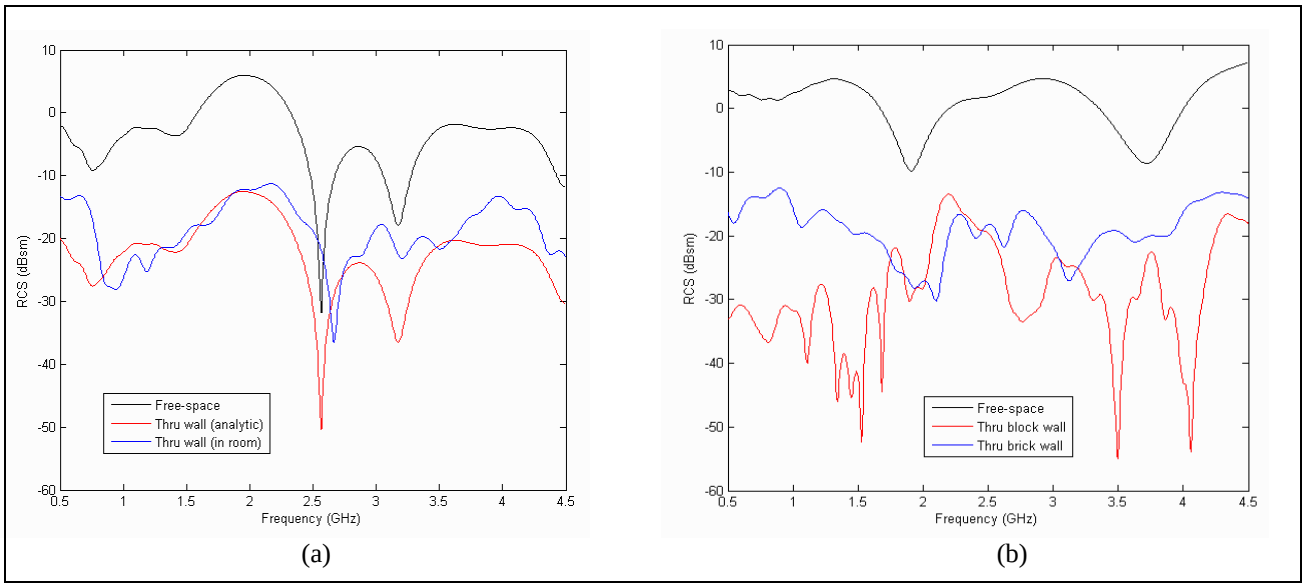

Figure 39. RCS of a standing human (the fit man from figure 2b), behind a 12 in. thick brick wall at 0° azimuth (front view) and 0° elevation, with (a) V-V and (b) H-H polarization, computed by two methods ("in room" and "analytic"), where the free-space RCS was plotted for comparison.

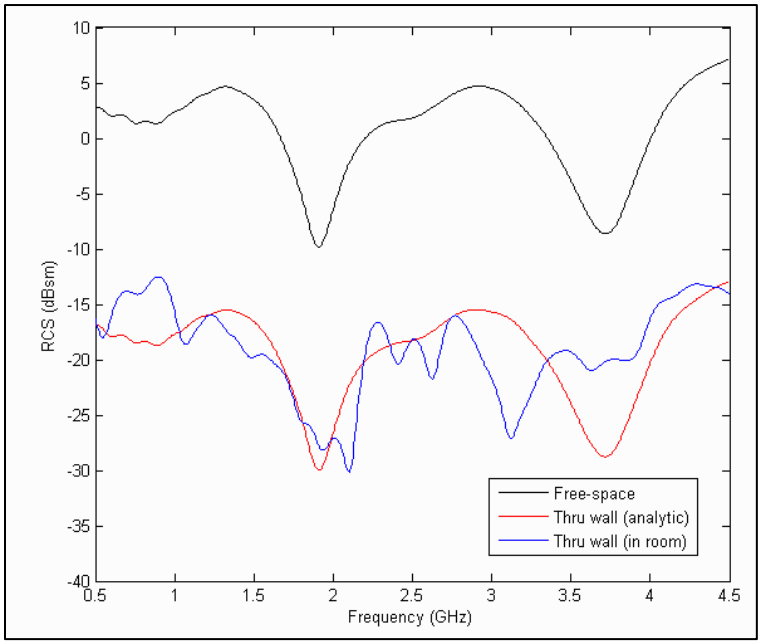

Figure 40. RCS of a standing human (the fit man from figure 2b) behind a 12 in. thick brick wall at 30° azimuth and 0° elevation with V-V polarization, computed by two methods ("in room" and "analytic"); the free-space RCS was plotted for comparison.

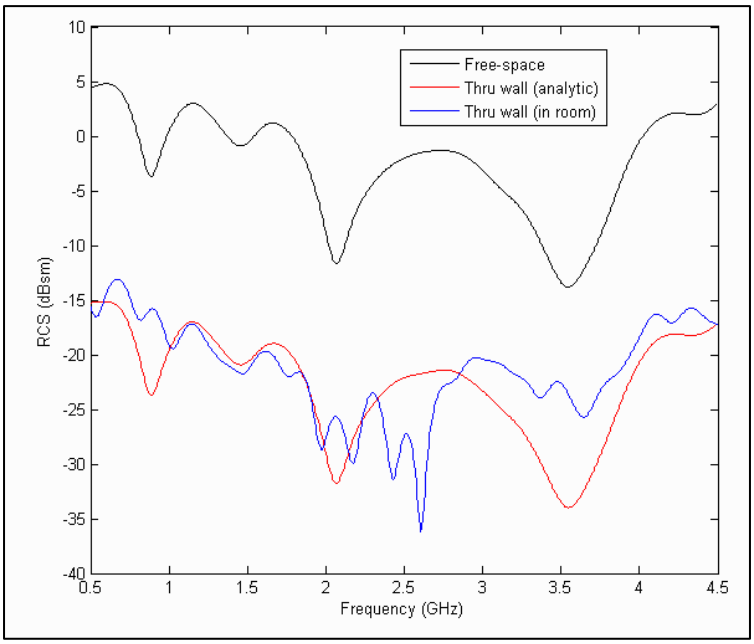

Figure 41. RCS of a standing human (the fit man as shown in figure 2b) behind a 12 in. thick cinder block wall at 0° azimuth and 0° elevation with V-V polarization, computed by the "in room" method (red line); the free-space RCS (black) and the RCS behind a brick wall (blue) were plotted for comparison.

4. Conclusions

The UWB microwave radar for through-the-wall sensing and imaging is a promising technology with important military applications, and consequently, has received a great deal of attentions from defense agencies in many countries. Although a number of such radar systems are currently being developed, there are still many unknowns related to their operation, performance, and effectiveness. An important application of the STTW radar constitutes the detection, classification, and tracking of personnel inside building structures. The work presented here consists of computer models of the human body radar signature, with applications to STTW scenarios.

In section 3, we conducted a fairly thorough investigation in modeling a stationary human body in various positions in free-space over a ground plane or behind a wall. First, we analyzed a number of issues regarding the accuracy and validity of our FDTD models of the human body radar signature. Next, we presented the simulation results as RCS versus frequency and aspect angle, and the statistics of the human RCS with respect to orientation were analyzed. Our models show that the average human body RCS (computed over all aspect angles) varies in a tight range (from -4 to 0 dBsm), in the frequency range of interest for STTW radar, and it is not

very sensitive to the body type or position. We also presented a series of SAR images of the human body in free-space, explaining the features apparent in these images. When the human was equipped with a long metallic stick (simulating a rifle barrel), we noticed interesting polarization effects in the radar signature, also clearly reflected in the SAR images. Finally, we presented two different methods of computing the RCS of a human behind a wall and suggested what type of scenario requires employing either of the two.

The conclusion is that the human body generally has a fairly large radar signature, which can be detected through many types of wall structures. However, the major issue is being able to discriminate a human body signature from that of other objects present in a room. At the current stage of our work, it is difficult to identify salient features of a stationary human that provide enough information to an automatic target recognition engine searching for the human presence in such an environment. Nevertheless, as we demonstrated in section 3.2, the average RCS (over aspect angle) of a human body is consistently bounded within a fairly tight range, which may facilitate the target prescreening process based on the radar signature magnitude alone. This could be particularly exploited in a SAR image, where the pixel intensity at the target location is a function of the angular average of that target's return. It is very likely that a through-the-wall human body detection scheme will eventually have to rely on analyzing the Doppler signature of the human motion, or may require the development of moving target indicator (MTI) techniques based on SAR image changes. These will constitute some major directions of our future research work at ARL in the context of the STTW programs.

References

1. Carin, L.; Geng, N.; McClure, M.; Sichina, J.; Nguyen, L. Ultra-wide band synthetic aperture radar for mine-field detection. *IEEE Antennas and Propagation Magazine* **February 1999**, *41* (1), 18–33.

2. Ressler, M. A.; McCorkle, J. W. Evolution of the Army Research Laboratory ultra-wideband test bed. In *Ultra-Wideband Short-Pulse Electromagnetics 2*, L. Carin and L.B. Felsen eds., Plenum Press, New York, 1995, 109–123.

3. Yee, K. S. Numerical solution of initial boundary value problems involving Maxwell's equations in isotropic media. *IEEE Transactions on Antennas and Propagation* **May 1966**, *14*, 302–307.

4. Taflove, A.; Hagness, S. C. *Computational Electrodynamics: The Finite-Difference Time-Domain*, Artech House, Boston, MA, 2000.

5. Kunz, K.; Luebbers, R. *The Finite-Difference Time-Domain Method for Electromagnetics*, CRC Press, Boca Raton, FL, 1993.

6. ARL MSRC Web page. http://www.arl.hpc.mil (accessed August 2007).

7. Lazzi, G.; Pattnaik, S.; Furse, C.; Gandhi, O. Comparison of FDTD computed and measured radiation patterns of commercial mobile telephones in presence of the human head. *IEEE Transactions on Antennas and Propagation* **June 1998**, *46*, 943–944.

8. Tinniswood, A.; Furse, C.; Gandhi, O. Computations of SAR distributions for two anatomically based models of the human head using CAD files of commercial telephones and the parallelized FDTD code. *IEEE Transactions on Antennas and Propagation* **June 1998**, *46*, 829–833.

9. Toftgard,J;. Hornsleth, S.; Andersen, J. Effects of portable antennas in the presence of a person," *IEEE Transactions on Antennas and Propagation* **June 1993**, *41*, 739–746.

10. Brooks Air Force Base Web page. http://www.brooks.af.mil (accessed September 2003).

11. Gabriel, C. Compilation of the dielectric properties of body tissue at RF and microwave frequencies. *USAF School Aerospace Med.*, Brooks AFB, TX, AL/OE-TR-1996-0037, 1996.

12. 3D CAD Browser Web page. http://3dcadbrowser.com (accessed July 2005).

13. Remcom Web page. http://www.remcom.com (accessed November 2006).

14. Autodesk Web page. http://www.autodesk.com/maya (accessed June 2007).

15. E. Knott, J. Shaeffer and M. Tuley, *Radar Cross Section*, Artech House, Boston, MA, 1993.

16. HyPerComp, Inc., Web page. http://www.hypercomp.net (accessed May 2007).

17. Skolnik, M. I. *Introduction to Radar Systems*, McGraw Hill, New York, 2001.

18. Balanis, C. *Advanced Engineering Electromagnetics*, Wiley, New York, 1989.

19. Soumekh, M. *Synthetic Aperture Radar Signal Processing*, Wiley, New York, 1999.

20. Oppenheim, A. V.; Schafer, R. W. *Discrete-Time Signal Processing*, Prentice Hall, Englewood Cliffs, NJ, 1989.

21. Hubral P.; Tygel, M. Analysis of the Rayleigh pulse. *Geophysics* **1989**, *54*, 654–658.

22. Shaeffer, J. F.; Hom, K. W.; Baucke, R. C.; Cooper, B. A.; Talcott, N. A. *Bistatic k-space imaging for electromagnetic prediction codes for scattering and antennas*; Technical Paper NASA-TP-3569; National Aeronautics and Space Administration: Langley, VA, July 1996.

Acronyms

ARL	U.S. Army Research Laboratory
CAD	Computer-Aided Design
CEM	computational electromagnetics
CERDEC	Communications-Electronics Research Development and Engineering Center
CPU	central processing unit
DC	direct current
DoD	Department of Defense
FDTD	Finite Difference Time Domain
FOPEN	foliage penetrating radar
GPR	ground penetrating radar
H-H	horizontal-horizontal
HPC	High-Performance Computing
I2WD	Intelligence and Information Warfare Directorate
MSRC	Major Shared Resource Center
MTI	moving target indicator
ONR	Office of Naval Research
RCS	radar cross section
RF	radio frequency
SAIC	Science Applications International Corporation

SAR	synthetic aperture radar
STTW	sensing through the wall
TEMPUS	Time-Domain Electro-Magnetic Parallel Unstructured Simulator
UWB	ultra-wideband
V-V	vertical-vertical

Distribution List

No. of Copies	Organization
1	ADMNSTR
PDF	DEFNS TECHL INFO CTR ATTN DTIC OCP (ELECTRONIC COPY) 8725 JOHN J KINGMAN RD STE 0944 FT BELVOIR VA 22060-6218
1	DARPA ATTN IXO S WELBY 3701 N FAIRFAX DR ARLINGTON VA 22203-1714
1	OFC OF THE SECY OF DEFNS ATTN ODDRE (R&AT) THE PENTAGON WASHINGTON DC 20301-3080
1	US ARMY RSRCH DEV & ENGRG CMND ARMAMENT RSRCH DEV & ENGRG CTR ARMAMENT ENGRG & TECHNLGY CTR ATTN AMSRD AAR AEF T J MATTS BLDG 305 APG MD 21005-500
1	US ARMY TRADOC BATTLE LAB INTEGRATION & TECHL DIRCTRT ATTN ATCD B 10 WHISTLER LANE FT MONROE VA 23651-5850
3	US ARMY RDECOM CERDEC I2WD ATTN AMSRD CER IW IM W CHIN BLDG 600 MCAFEE CENTER FT MONMOUTH NJ 07703
1	PM TIMS PROFILER (MMS P) AN/TMQ 52 ATTN B GRIFFIES BUILDING 563 FT MONMOUTH NJ 07703
1	SMC/GPA 2420 VELA WAY STE 1866 EL SEGUNDO CA 90245-4659
1	US ARMY INFO SYS ENGRG CMND ATTN AMSEL IE TD F JENIA FT HUACHUCA AZ 85613-5300
1	COMMANDER US ARMY RDECOM ATTN AMSRD AMR W C MCCORKLE 5400 FOWLER RD REDSTONE ARSENAL AL 35898-5000
1	US ARMY RSRCH LAB ATTN AMSRD ARL CI OK TP TECHL LIB T LANDFRIED BLDG 4600 APG MD 21005-5066
1	OFFICE OF NAVAL RSRCH ATTN M KRUEGER ONE LIBERTY CENTER 875 N RANDOLPH ST STE 1425 ARLINGTON VA 22203-1995
1	US NAVAL RSRCH LAB RADAR DIV ADAPTIVE PROCESSING SECTION ATTN A DESROSIERS 4555 OVERLOOK AVE SW WASHINGTON DC 20375-5312
1	US GOVERNMENT PRINT OFF DEPOSITORY RECEIVING SECTION ATTN MAIL STOP IDAD J TATE 732 NORTH CAPITOL ST NW WASHINGTON DC 20402
1	DIRECTOR US ARMY RSRCH LAB ATTN AMSRD ARL RO EV W D BACH PO BOX 12211 RESEARCH TRIANGLE PARK NC 27709

No. of Copies	Organization
18	US ARMY RSRCH LAB ATTN AMSRD ARL D J M MILLER ATTN AMSRD ARL CI OK T TECHL PUB (2 COPIES) ATTN AMSRD ARL CI OK TL TECHL LIB (2 COPIES) ATTN AMSRD ARL SE RM W O COBURN ATTN AMSRD ARL SE RU A SULLIVAN ATTN AMSRD ARL SE RU C LE ATTN AMSRD ARL SE RU G GAUNAURD ATTN AMSRD ARL SE RU J SICHINA ATTN AMSRD ARL SE RU K KAPPRA ATTN AMSRD ARL SE RU L NGUYEN ATTN AMSRD ARL SE RU M RESSLER ATTN AMSRD ARL SE RU T DOGARU (4 COPIES) ATTN IMNE ALC IMS MAIL & RECORDS MGMT ADELPHI MD 20783-1197
35	TOTAL (1 elec, 34 hard copies)

INTENTIONALLY LEFT BLANK.